Modelling Flow of Cerebrospinal Fluid

Almut Eisenträger

almut.eisentraeger@sjc.ox.ac.uk

St John's College
University of Oxford

21st October 2009

Contents

1 The Cerebrospinal Fluid System

1.1 Normal Physiology

In a healthy human brain, cerebrospinal fluid (CSF), a water-like liquid, fills a system of cavities, known as ventricles, inside the brain and also surrounds the brain, mechanically stabilising it by decreasing forces such as gravity on the brain tissue through the buoyant effect. Besides, CSF serves as a space reservoir inside the rigid skull. For example, arterial blood which is pumped into the brain with each heartbeat takes up space made available by other fluid leaving the brain, this being partly venous blood and partly CSF. Furthermore, CSF is likely to have chemical importance, including the regulation of the extracellular environment of neurons and transportation of hormones, nutrients, and waste products through the nervous system.

The production of CSF mainly takes place at the choroid plexuses of the ventricles. It is formed by an active secretion from arterial blood at a relatively constant rate of 500 ml per day, independent of arterial blood pressure and CSF pressure, so that the total volume of CSF, on average 150 ml, within and around the brain and spinal cord is renewed about three times a day.

The two lateral ventricles, one in each hemisphere, make up most of the ventricular space, which itself contains only a fraction of the total CSF volume. CSF formed in the lateral ventricles flows into the third ventricle, through a long thin channel, known as the aqueduct of Sylvius, and into the forth ventricle. From there it leaves the ventricular system, some flowing down around the spinal cord, some around the brain, filling the so-called subarachnoid space between the arachnoid, which is attached to the skull via the dura mater, and the pia mater, covering the brain surface (Fig. 1).

From the subarachnoid space, CSF is absorbed into the venous sinuses through the arachnoid villi, which work as one-way-valves. If the CSF pressure is higher than the pressure in the sinuses, CSF enters venous blood at a rate linearly dependent on the pressure difference. Should venous blood pressure exceed CSF pressure, though, no fluid is exchanged. All the CSF movements within and around the brain and spinal cord should not be considered as slow and steady but oscillatory, due to the pressure and volume pulsations of cerebral blood with each heartbeat (Nolte, 2002).

1.2 Hydrocephalus

Disturbances of the CSF circulation can cause brain diseases such as hydrocephalus, normal pressure hydrocephalus (NPH) or benign intracranial hypertension (BIH). Hydrocephalus is characterised by the accumulation of CSF in enlarged ventricles, often accompanied by oedemas in the surrounding brain tissue, together with an increased intracranial pressure (ICP), that is CSF pressure. In children this also leads to an enlargement of the head, whereas in adults the rigidity of the skull impedes this.

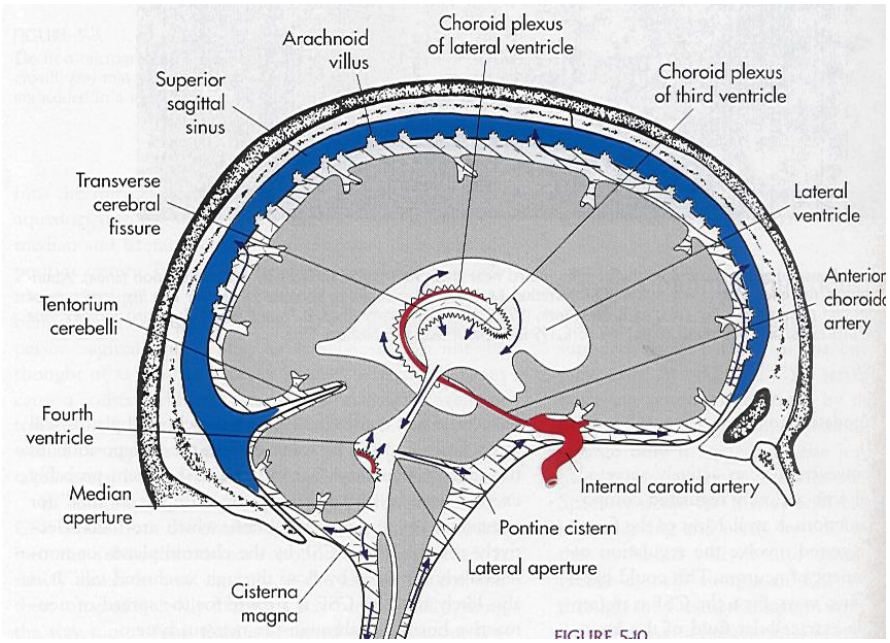

Fig. 1: Normal CSF flow path (Nolte, 2002, p. 104)

The most common cause for hydrocephalus, in this case called noncommunicating, is an obstruction of the normal CSF flow path, for example due to a tumour or after head injury. The causes for communicating hydrocephalus could be an overproduction of CSF or an increased resistance to CSF absorption into the sinuses. In NPH, the ventricles are enlarged without apparent increase of the pressure, BIH is the opposite phenomenon, an increased ICP and ventricles of normal or even reduced size. Both, the displacement of the brain tissue and the increased ICP, induce stresses in the brain tissue that can have fatal consequences for the patient. The conditions NPH and BIH still are only poorly understood. Once diagnosed, hydrocephalus can often be treated successfully either by removal of the obstruction in the pathway or by insertion of a shunt, a tube with a valve for removal of CSF from the ventricles into other parts of the body.

1.3 The Infusion Test

Next to imaging techniques showing the size and form of the ventricles, the so-called infusion test is a standard test to get an insight into the CSF circulation in hydrocephalic patients. For this test, additional fluid is injected into the CSF space at a constant rate while continuously measuring the CSF pressure. The injection could be either into the ventricles or into the lumbar space. From the gradual pressure increase and the new equilibrium, usually reached after 10–20 minutes, parameters such as the resistance to CSF absorption can be derived and used to help with decisions about shunt surgery (Czosnyka et al., 2004).

1.4 Aim of Research

Despite the quite common occurrence of hydrocephalus, at about one in 2000 births (see `http://www.cureresearch.com/h/hydrocephalus/stats.htm`), not counting hydrocephalus in older children or adults, CSF dynamics is not yet well understood and current models can only explain some aspects. So, the aim of mathematical research in this field is to gain a better understanding of the mechanical behaviour of the brain and the CSF circulation and to find models that accurately describe these. Most models for CSF circulation that are available are quasi-steady, intended for time scales of days and weeks to describe the development of hydrocephalus. We focus on a biomechanical simulation of CSF flow using the theory of poroelasticity and trying to include time dependence in a way that CSF dynamics can also be predicted on time scales of minutes, the duration of the infusion test, down to fractions of seconds to be able to capture CSF pulsations at heart frequency as well.

This report describes the steps towards such a simulation that we have taken so far. First, we review the main modelling approaches for CSF circulation, hydrocephalus, and the infusion test in section 2. In section 3, the results of least squares parameter fits of compartment models to different sets of clinical measurements of the infusion test are described and explained. As a first step towards a finite element simulation of the poroelastic model of the brain, we have examined a one-dimensional poroelastic model problem, described in section 4. Finally, we give an outlook on the further research in section 5.

2 Models of CSF Flow

2.1 Compartment Models

Already over two centuries ago, the coupling between volumes of CSF and blood in the brain, due to its enclosure in the rigid skull, was noticed by medical researchers (Monro, 1783). An increase of volume in one of the compartments has to be accompanied by a decrease of the volume in the other. Forty years later, Kellie (1824) refined this model by differentiating further between venous and arterial blood.

Compartment models of CSF describe this coupling using the similarity with electric circuits. Resistances between compartments and compliances, defined as the derivative of the volume-pressure curve in the different compartments, are equivalent to electrical resistances and capacities. Early authors (Guinane, 1972) still assumed the compliance to be constant, but after many studies in the 1970's, either by experiments on animals or by analysis of the data from infusion tests in patients, to examine the form of the volume-pressure curve, a consensus was reached, describing the compliance in the form

$$C = \frac{\mathrm{d}V}{\mathrm{d}p} = \frac{1}{E\,(p - p_{\mathrm{r}})} \tag{1}$$

with a brain elasticity E and a reference pressure p_r. The importance and the value of p_r are still subject to discussion. Some authors take it to be atmospheric pressure (Marmarou et al., 1978), others choose the pressure in the sagittal sinus (Juniewicz et al., 2005), Wirth and Sobey (2008) suggest that it is related to the pressure in and stiffness of the bridging veins. With (1), an ordinary differential equation for the CSF pressure $p(t)$ can be derived from the volume balance

$$\frac{\mathrm{d}V}{\mathrm{d}t} = Q_\mathrm{in}(t) - Q_\mathrm{out}(t),$$

where the inflow of CSF equals the sum of the constant production rate and a possible infusion rate and the outflow is linearly dependent on the pressure difference between CSF and venous blood in the sagittal sinus with resistance R. From the chain rule

$$\frac{\mathrm{d}V}{\mathrm{d}t} = \frac{\mathrm{d}V}{\mathrm{d}p}\frac{\mathrm{d}p}{\mathrm{d}t} = C\frac{\mathrm{d}p}{\mathrm{d}t},$$

we thus obtain

$$\frac{1}{E\,(p - p_\mathrm{r})}\frac{\mathrm{d}p}{\mathrm{d}t} = Q_\mathrm{prod} + Q_\mathrm{inf} - \frac{p - p_\mathrm{ss}}{R}. \tag{2}$$

A review of compartment models as well as poroelasticity models (see §2.2) of CSF flow up to that point can be found in Tenti et al. (2000).

Many variations of compartment models have been developed since. One example is the approach by Egnor et al. (2001, 2002), who, inspired by elastic models of hydrocephalus, derived an oscillatory single-compartment model of the CSF-blood interaction and proposed disturbances of the CSF pulsations to be the cause of communicating hydrocephalus. Cirovic et al. (2003), on the other hand, developed a model with five compartments, one for CSF, one for arterial blood, and three for different parts of the venous bed, to study the CSF compliance and concluded that it mainly consists of the compliance of the venous bed due to the collapsibility of veins. An analytic solution to (2) from the single compartment model before, during and after an infusion test can be found in Juniewicz et al. (2005), where least squares parameter fits are used to study the phenomenon of increased CSF pressure after the test. Some authors try to improve compartment models without increasing the computational effort too much by incorporating only certain aspects of biomechanical models (Linninger et al., 2005, 2009b).

Despite numerous studies, the complexity of CSF dynamics has neither been completely understood nor can it be fully captured by compartment models. Even basic assumptions have not been verified completely, as Andersson et al. (2008) pointed out, who questioned the linearly pressure dependent CSF outflow and found a nonlinear tendency for pressures above the normal range, which might influence the results of clinical measurements like the infusion test.

Nevertheless, compartment models are important due to their relative simplicity and sufficiently good results in normal circumstances, so that they are used everyday in

clinics to interpret the results of various clinical measurements to examine CSF dynamics (Czosnyka et al., 2004), especially to help decide about shunt surgery for hydrocephalic patients. However, their main drawback is that they have no spatial variation. They cannot be used to compute the stresses inside the brain tissue, which are actually responsible for tissue damage, nor can they predict the size or the form of the ventricles. Therefore, researchers started searching for biomechanical approaches to model the CSF flow through the brain.

2.2 Poroelastic Models

Hakim et al. (1976) were the first to use the approach of biomechanical modelling on CSF dynamics and hydrocephalus. Although they only used the equations for modelling an elastic solid, their description of the brain as an "open cell sponge made of viscoelastic material" was the starting point for poroelastic modelling of the brain. Nagashima et al. (1987) picked up this idea and developed a two-dimensional model and numerical simulation of the onset of hydrocephalus using the theory of poroelasticity or consolidation theory, as Biot (1941) called it originally. Compared to clinical observations, their results were in qualitative agreement. The quantitative accuracy was nevertheless limited by inaccurate material parameter values and the boundary conditions used.

Analytic solutions in simplified geometries, such as the one proposed by Kaczmarek et al. (1997) for the steady state in cylindrical geometry, including a strain dependent permeability, help understand the general behaviour of the governing equations and can be used to benchmark numerical models. Two of the main challenges for research in hydrocephalus were pointed out in the review paper of Tenti et al. (2000) as finding "a suitable nonlinear constitutive equation (i. e. a relation between stress and strain) for the brain, in order to account for the large deformations typical of hydrocephalus" and deriving "an appropriate set of boundary conditions which would make the mathematical problem well posed."

Levine (1999) compares three hypotheses of governing equations and proposes that NPH can be explained by an effective absorption of CSF in the parenchyma, leading to only a small pressure gradient between the ventricles and the subarachnoid space. Similar effects would be expected if other fluid, such as blood or interstitial fluid, leaves the brain already due to a small pressure gradient and therefore changes the efficiency of pressure transmission through the porous brain tissue (Levine, 2008).

A three-dimensional, spherically symmetric poroelastic model was developed by Smillie et al. (2005), including a partly or completely obstructed aqueduct as well as a shunt. Building from there, Sobey and Wirth (2006) examined the effect of strain dependency in the permeability, which leads to a nonlinear problem. They also provided a link between poroelastic models and compartment models by deriving the compliance from mechanical principles. In their companion paper (Wirth and Sobey, 2006), more realistically shaped geometries were considered. Later, they extended these models with a

triphasic poroelastic approach, including arterial blood in addition to brain tissue and CSF. Restricting the model to a constant permeability, an analytic solution for the fully time-dependent spherically symmetric problem, including responses to blood pressure oscillations and the infusion test, was proposed in Wirth and Sobey (2009).

Detailed brain images can be used to build patient-specific models and verify simulated flow patterns as was done by Linninger et al. (2007, 2009a). Still, the limitations due to unknown variations of the brain tissue material parameters spatially, variations between patients or with age, persist despite the accurate geometry.

2.3 Viscoelastic Models

Another approach taken for the modelling of hydrocephalus treats the brain as a viscoelastic material. Miller (1998) argues that biphasic approaches modelling the solid phase as a hyperelastic material cannot accurately describe certain compression tests of soft biological tissue, where energy dissipation is observed . Instead a linear single phase viscoelastic model is proposed for brain tissue (Miller, 1999). Taylor and Miller (2004) then use this viscoelastic model for the solid matrix in a biphasic model of the parenchyma together with poroelastic principles to reassess Young's modulus of brain tissue for the slowly developing hydrocephalus. They arrive at a value of 584 Pa, about one order of magnitude lower than those previously cited in the literature. A poroviscoelastic model for soft biological tissue using the most general viscoelastic model, the generalised Maxwell model, for the solid phase and including strain dependent permeability can be found in Ehlers and Markert (2000).

Sivaloganathan et al. (2005a), on the other hand, treat the brain parenchyma as a thick-walled cylindrical tube made of an impermeable viscoelastic solid ("standard solid") with given constant pressures at the inner and outer boundaries. Due to the simple geometry and a quasi-static approach, the analytic solution of this problem can be found from the solution of an elastic problem via the correspondence principle. An extension of this model with oscillatory pressure boundary conditions or even the problem with zero displacement at the outer boundary is presented in Sivaloganathan et al. (2005b).

As with poroelastic models, unknown or inaccurate values of material parameters limit the accuracy of the results of viscoelastic or poroviscoelastic models of the brain. Cheng et al. (2008) review methods of retrieving these parameters and show how different procedures can lead to such varied results.

3 Parameter Fits to Infusion Tests

3.1 Motivation

As a preparation to be able to simulate the infusion test using a poroelastic model, we have examined some clinical measurements of infusion tests by fitting the parameters

for single compartment type models similar to (2) to the data. These models give a locally time averaged prediction of mean ICP that neglects oscillation on the time scale of heartbeats. For convenience, figures related to this section are gathered in appendices A.1 and A.2.

3.2 Models of mean ICP

3.2.1 Constant Elasticity

Juniewicz et al. (2005) use the following differential equation as a model for the mean intracranial pressure $p(t)$

$$\frac{p'(t)}{E\,(p(t)-p_\mathrm{r})}+\frac{p(t)-p_\mathrm{b}}{R}=Q(t), \tag{3}$$

where E is the constant cerebral elasticity and R the resistance to absorption of cerebrospinal fluid into the sagittal sinus. The reference pressure p_r is assumed to be equal to the pressure in the sagittal sinus and the baseline pressure p_b, i. e. the mean ICP before the infusion starts, already incorporates the production rate of CSF via

$$Q_\mathrm{prod}=\frac{p_\mathrm{b}-p_\mathrm{r}}{R}.$$

Furthermore, the infusion rate is given as

$$Q(t)=\begin{cases}0 & \text{before infusion, i. e. } (t_1\le t\le t_2),\\ Q_\mathrm{inf} & \text{during infusion, i. e. } (t_2\le t\le t_3),\\ 0 & \text{after infusion, i. e. } (t_3\le t\le t_4).\end{cases}$$

Using this, the ordinary differential equation (3) can be rewritten as

$$p'(t)=\begin{cases}-\frac{E}{R}\,(p(t)-p_\mathrm{r})\,(p(t)-p_\mathrm{b}) & (t_1\le t\le t_2),\\ -\frac{E}{R}\,(p(t)-p_\mathrm{r})\,(p(t)-(p_\mathrm{b}+RQ_\mathrm{inf})) & (t_2\le t\le t_3),\\ -\frac{E}{R}\,(p(t)-p_\mathrm{r})\,(p(t)-p_\mathrm{b}) & (t_3\le t\le t_4),\end{cases} \tag{4}$$

which, given the initial condition $p(t_1)=p_\mathrm{b}$, yields the solution

$$p(t)=\begin{cases}p_\mathrm{b} & (t_1\le t\le t_2),\\ p_\mathrm{r}+\frac{(p_\mathrm{b}-p_\mathrm{r})(RQ_\mathrm{inf}+p_\mathrm{b}-p_\mathrm{r})}{(p_\mathrm{b}-p_\mathrm{r})+RQ_\mathrm{inf}\exp\left(-\frac{E}{R}(RQ_\mathrm{inf}+p_\mathrm{b}-p_\mathrm{r})(t-t_2)\right)} & (t_2\le t\le t_3),\\ p_\mathrm{r}+\frac{(p_\mathrm{b}-p_\mathrm{r})}{1+D\exp\left(-\frac{E}{R}(p_\mathrm{b}-p_\mathrm{r})(t-t_3)\right)} & (t_3\le t\le t_4),\end{cases} \tag{5}$$

where

$$D = \frac{p_\mathrm{b} - p_\mathrm{r}}{p(t_3^-) - p_\mathrm{r}} - 1$$

establishes continuity at time $t = t_3$.

3.2.2 Pressure-Dependent Elasticity

Wirth and Sobey (2008), on the other hand, propose a pressure dependent elasticity

$$E = \tilde{e}\left(p(t) - p_\mathrm{r}\right)^{n-1},$$

with an unknown power n resulting in the nonlinear ordinary differential equation for mean ICP

$$p'(t) = \begin{cases} -\frac{\tilde{e}}{R}\left(p(t) - p_\mathrm{r}\right)^n \left(p(t) - p_\mathrm{b}\right) & (t_1 \le t \le t_2), \\ -\frac{\tilde{e}}{R}\left(p(t) - p_\mathrm{r}\right)^n \left(p(t) - (p_\mathrm{b} + RQ_\mathrm{inf})\right) & (t_2 \le t \le t_3), \\ -\frac{\tilde{e}}{R}\left(p(t) - p_\mathrm{r}\right)^n \left(p(t) - p_\mathrm{b}\right) & (t_3 \le t \le t_4), \end{cases} \tag{6}$$

which cannot, in general, be solved in closed form. Nevertheless, we get analytic solutions for $n = 1$, namely (5), and for $n = 0$, that is

$$p(t) = \begin{cases} p_\mathrm{b} & (t_1 \le t \le t_2), \\ p_\mathrm{b} + RQ_\mathrm{inf} - RQ_\mathrm{inf} \exp\left(-\frac{\tilde{e}}{R}\left(t - t_2\right)\right) & (t_2 \le t \le t_3), \\ p_\mathrm{b} + \left(p(t_3^-) - p_\mathrm{b}\right) \exp\left(-\frac{e}{R}\left(t - t_3\right)\right) & (t_3 \le t \le t_4). \end{cases}$$

For arbitrary values of n, a solution is obtained numerically with the solver `ode45` in MATLAB for initial value problems. In both cases, we numerically obtain an approximation of the increase in CSF volume at the end of the infusion from

$$\begin{aligned} \Delta V &= \int_{t_1}^{t_3} Q_\mathrm{in}(t) - Q_\mathrm{out}(t)\mathrm{d}t \\ &= \int_{t_1}^{t_3} Q_\mathrm{prod} + Q(t) - \frac{p(t) - p_\mathrm{r}}{R}\mathrm{d}t. \end{aligned}$$

3.3 Least Squares Parameter Fits

As can be seen from (5), the four parameters E, R, p_r and p_b uniquely identify the solution, but trying to fit them to measured data will lead to a badly conditioned optimisation problem, since for example the quotient E/R enters the function rather than E. This gets even worse as we include the variable power n. In an attempt to resolve this,

we consider an equivalent problem with the parameters

$$x_1 = \frac{p_\mathrm{b}}{p_\mathrm{b}^\mathrm{g}}, \qquad x_2 = \frac{\tilde{e}}{R}\frac{R^\mathrm{g}}{\tilde{e}^\mathrm{g}}, \qquad x_3 = \frac{p_\mathrm{r}}{p_\mathrm{r}^\mathrm{g}}, \qquad x_4 = \frac{RQ_\mathrm{inf} + p_\mathrm{b}}{R^\mathrm{g}Q_\mathrm{inf}^\mathrm{g} + p_\mathrm{b}^\mathrm{g}}, \qquad x_5 = n.$$

The guessed values with superscript g are computed from

$$\begin{aligned}
n^\mathrm{g} &= \begin{cases} n & \text{if } n \text{ is given} \\ 1 & \text{if } n \text{ is to be determined} \end{cases} \\
p_\mathrm{b}^\mathrm{g} &= \min p_\mathrm{avg}(t), \\
p_\mathrm{r}^\mathrm{g} &= \max\left(p_\mathrm{b}^\mathrm{g} - 4\,\mathrm{mmHg}, 1\,\mathrm{mmHg}\right), \\
R^\mathrm{g} &= \frac{\max p_\mathrm{avg}(t) - p_\mathrm{b}^\mathrm{g}}{Q_\mathrm{inf}}, \\
E^\mathrm{g} &= 0.25\,(\mathrm{ml})^{-1}, \\
\tilde{e}^\mathrm{g} &= E^\mathrm{g}\left(p_\mathrm{b}^\mathrm{g} - p_\mathrm{r}^\mathrm{g}\right)^{1-n^\mathrm{g}},
\end{aligned}$$

where $p_\mathrm{avg}(t)$ is the average of the measured pressure in a one minute interval starting at time t.

We define the objective function

$$F : \mathbb{R}^5 \mapsto \mathbb{R} : \quad x \mapsto \sum_{t\in\mathcal{T}} \left(p(t) - p_\mathrm{m}(t)\right)^2,$$

where $p(t)$ is the analytical or numerical solution to (6) and $\mathcal{T}$ is the set of all times at which ICP was measured, and consider the nonlinear minimisation problem

$$\min_x F(x)$$

in three versions

1. subject to $n = 1$ (in this case the analytic solution (5) can be used),
2. subject to $n = n_\mathrm{given} \neq 1$,
3. with variable n.

Each of these was implemented separately using `fminsearch` in MATLAB to exploit the knowledge of the analytic solution or the known value of n, hence avoiding constrained optimisation. During the minimisation procedure in cases 2 and 3, often such parameter sets were reached that made $(p - p_\mathrm{r})^n$ complex, so that the ODE solver returned a complex solution for the pressure curve, which could not be handled properly by the surrounding minimisation algorithm. An attempt to resolve this and similar problems with negative parameter values by the use of constrained optimisation with `fmincon` in MATLAB was hampered by the extreme increase in computation time to several weeks per data set. Furthermore, most of the parameter sets obtained from the

Set	t_1	t_2	t_3	t_4	Q_{inf}	ABP
00	0.0	5.5	19.9	24.0	1.50	86
01	0.0	6.7	13.7	26.7	1.50	107
02	0.0	5.4	34.4	36.3	1.50	68
03	9.0	15.3	34.8	38.7	1.50	52
04	0.0	8.3	24.8	31.8	1.50	67
05	0.0	8.0	19.0	27.5	1.50	70
06	12.0	14.8	39.8	47.1	1.50	93
07	0.0	12.7	26.7	27.0	1.50	125
08	0.0	13.0	27.0	31.7	1.50	68
09	0.0	4.0	13.0	23.9	1.00	85
10	0.0	4.5	20.5	26.0	1.50	57

Table 1: Input for least squares fits: Times (in min), infusion rate (in ml/min) and mean arterial blood pressure (in mmHg) of all data sets

constrained optimisation problem were not physically sensible either as they lay exactly on the boundary. In the following subsection, we only give results that produce real-valued pressure curves of the expected form.

3.4 Data and Results

Dr. Marek Czosnyka from Addenbrooke's Hospital, Cambridge, kindly provided us with several data sets of infusion tests. Those include measurements of CSF pressure, taken either from the ventricles or from the spinal column, and blood pressure at a rate of 30 data points per second over the whole duration of the test, that is approximately ten minutes before until ten minutes after the infusion, together with the infusion rate and the times when the infusion was started and stopped. The times, the infusion rate and the mean arterial blood pressure, averaged over the whole duration of the measurement, are given in Table 1. For data sets 03 and 06, the first few minutes of the measurement were not included in the parameter fits because of irregularities in the intracranial pressure curve most likely due to readjustments of the pressure sensor. Originally, the time after the infusion was included in the fits, but after we learned that some of the patients might have sat up after the infusion to improve their condition if side effects like headache or nausea appeared, we considered those measurements not trustworthy anymore and focussed on the time before and during the infusion.

The results of the three versions of the minimisation problem, where they were real valued and sensible, are given in Table 2. As is common in medical research, all pressure values are given in mmHg $\approx 133^{-1}$Pa.

The corresponding plots of the measured pressure curve, its best fit and an approximation of CSF inflow, outflow and volume change can be found in appendix A.1.

Set	vers	n	$\tilde{e}$	$E(p_\mathrm{b})$	R	p_r	p_b	Q_prod	ΔV
00	1	1.00	–	0.243	15.4	$2.13 \cdot 10^{+0}$	9.97	$5.08 \cdot 10^{-1}$	5.65
00	2	7.77	0.000	0.020	15.2	$-9.09 \cdot 10^{+1}$	9.99	$6.63 \cdot 10^{+0}$	5.45
00	3	0.50	1.249	0.908	15.6	$8.06 \cdot 10^{+0}$	9.95	$1.21 \cdot 10^{-1}$	5.83
01	1	1.00	–	0.166	455.4	$7.95 \cdot 10^{+0}$	14.83	$1.51 \cdot 10^{-2}$	10.32
02	1	1.00	–	0.156	4.2	$5.70 \cdot 10^{+0}$	6.17	$1.11 \cdot 10^{-1}$	17.02
03	1	1.00	–	0.361	10.2	$4.69 \cdot 10^{+0}$	7.75	$3.01 \cdot 10^{-1}$	4.96
03	2	0.55	1.297	2.607	10.2	$7.58 \cdot 10^{+0}$	7.79	$2.10 \cdot 10^{-2}$	5.04
03	3	0.50	1.436	5.076	10.2	$7.71 \cdot 10^{+0}$	7.79	$7.86 \cdot 10^{-3}$	5.06
04	1	1.00	–	0.526	5.2	$1.07 \cdot 10^{+1}$	11.47	$1.45 \cdot 10^{-1}$	4.62
04	2	5.76	0.000	0.038	5.2	$-4.95 \cdot 10^{+0}$	11.47	$3.18 \cdot 10^{+0}$	4.67
05	1	1.00	–	0.000	8.7	$-2.15 \cdot 10^{+5}$	11.46	$2.48 \cdot 10^{+4}$	8.82
05	3	0.30	0.021	0.000	8.7	$-5.68 \cdot 10^{+5}$	11.46	$6.55 \cdot 10^{+4}$	8.82
06	1	1.00	–	0.119	12.4	$2.78 \cdot 10^{+0}$	7.56	$3.85 \cdot 10^{-1}$	13.24
06	2	8.61	0.000	0.008	12.1	$-6.96 \cdot 10^{+1}$	7.60	$6.37 \cdot 10^{+0}$	12.70
07	1	1.00	–	0.478	11.0	$7.86 \cdot 10^{+0}$	8.43	$5.16 \cdot 10^{-2}$	7.12
07	2	4.08	0.000	0.045	10.7	$-2.72 \cdot 10^{+0}$	8.44	$1.04 \cdot 10^{+0}$	6.85
08	1	1.00	–	0.078	11.8	$-1.29 \cdot 10^{+1}$	8.05	$1.78 \cdot 10^{+0}$	7.52
08	3	0.50	0.490	0.140	12.0	$-4.24 \cdot 10^{+0}$	8.04	$1.02 \cdot 10^{+0}$	7.72
09	1	1.00	–	0.379	47.6	$1.91 \cdot 10^{+1}$	20.39	$2.66 \cdot 10^{-2}$	7.64
10	1	1.00	–	0.000	14.2	$-1.38 \cdot 10^{+6}$	12.59	$9.75 \cdot 10^{+4}$	12.73

Table 2: Results of least squares parameter fits with $[\tilde{e}] = \mathrm{mmHg}^{1-n} \cdot \mathrm{ml}^{-1}$, $[E(p_\mathrm{b})] = \mathrm{ml}^{-1}$, $[R] = \mathrm{mmHg} \cdot \mathrm{min} \cdot \mathrm{ml}^{-1}$, $[p_\mathrm{r}] = [p_\mathrm{b}] = \mathrm{mmHg}$, $[Q_\mathrm{prod}] = \mathrm{ml} \cdot \mathrm{min}^{-1}$, $[\Delta V] = \mathrm{ml}$

In some cases, we obtain parameter values that are several orders of magnitude smaller or larger than expected, usually simultaneously but reciprocally for E and p_r. This is due to their interplay in the compliance and shows how badly conditioned this least squares problem can be. This behaviour will be investigated further in the following subsection.

3.5 Parameter Variations

In order to look more closely at the behaviour of solutions to the model equation (6), we now vary the values for E, R, p_r, p_b and n around the standard parameter values given in Table 3 to examine their influence on the mean intracranial pressure curve. Again, where possible, we use the analytic solution (5), otherwise a numerical solution of (6) from MATLAB's `ode45`. Due to the big number of plots, they are again put in the appendix (A.2). In each plot, the mean ICP, flow rates and fluid content obtained from the standard values are plotted with a thick solid line and the variations with thin lines of various styles.

Start time of data	t_1	=	0	min
Start time of infusion	t_2	=	5	min
End time of infusion	t_3	=	20	min
End time of data	t_3	=	25	min
Infusion rate	Q_{inf}	=	1.5	$\text{ml} \cdot (\text{min})^{-1}$
Elasticity	E	=	0.2	$(\text{ml})^{-1}$
Resistance	R	=	15	$\text{mmHg} \cdot \text{min} \cdot (\text{ml})^{-1}$
Reference pressure	p_{r}	=	5	mmHg
Baseline pressure	p_{b}	=	10	mmHg

Table 3: Standard values before parameter variation

In the case $n = 1$, mainly the elasticity E (Fig. 29) defines the slope of the increasing pressure curve during the infusion and the decreasing pressure curve after the infusion. An increase in E increases the steepness, hence the new steady plateau is reached quicker. Nevertheless, the reference pressure has some influence as well, changing the shape of the slope and additionally the CSF production rate (Fig. 30). Adding the same value to both, the reference pressure and the baseline pressure, only shifts the pressure curve up or down without any effect on its shape or on the flow and volume curves (Fig. 31). A change in the baseline pressure can be regarded as such a shift together with a change of the reference pressure (Fig. 32). An increase in the outflow resistance R increases the pressure at the plateau, which is obvious from the volume balance in the new steady state $p_{\text{plateau}} - p_{\text{b}} = RQ_{\text{inf}}$ (Fig. 33). When keeping the production rate constant at the same time, this results in the same increase in plateau pressure, with a different shape due to the changed reference pressure, but in this case, the inflow, outflow and volume balance do not change with R (Fig. 34). Variations in n (Fig. 35) or both, n and $\tilde{e}$ (Fig. 36), have similar effects to the pressure curve as changes in the constant E, which is expected, as they are closely related.

3.6 Summary

Both, the results in §3.4 and the parameter variations in §3.5, indicate the very bad conditioning of this optimisation problem of fitting the parameter values of compartment models to clinical measurements. The example in Figure 37 makes this even more explicit. Two sets of different parameter values yield extremely similar shapes of the ICP, flow and volume curves. These values were only chosen by hand. Using one set as a starting guess for a least squares fit to the ICP curve of the other set, would probably lead to even closer results. The objective function F is very likely to have numerous local minima. Hence, the outcome of the fit highly depends on the starting guess of the parameter values. Obtaining the correct values for all five parameters through such a least squares fit to real clinical data without any further knowledge of the patient's pathological situation, thus, should be considered impossible.

4 Model Problem: Poroelasticity in 1D

4.1 Motivation

Since compartment models cannot fully capture the complexity of CSF dynamics, we want to find a suitable biomechanical model. Building from the ideas of Wirth and Sobey (2009), we want to explore the possibilities of modelling CSF dynamics with a generalised poroelastic approach. As a first step towards this, we consider a one dimensional poroelastic model problem with strain dependent permeability and derive a finite element simulation for this nonlinear problem. This will help us understand the behaviour of the governing equations and will, in addition, be useful for other applications, for example to model the flow of nutrient solution through a porous skeleton for the growth of cells in tissue engineering.

4.2 Model Equations

4.2.1 Governing Equations

We examine the following model problem. Consider an infinite layer of thickness L of an isotropic porous elastic solid filled with an incompressible fluid. The governing equations can be derived from the principles set out in Biot (1941), or found in more recent books about poroelasticity (Wang, 2000; Coussy, 2004). Each volume element is assumed to contain both solid and fluid, so that the stress is a combination of the elastic stress of the solid and the pressure p of the fluid. With linear elasticity, the strain becomes $\varepsilon = \frac{\partial u}{\partial x}$, where u is the displacement of the solid. Neglecting body forces and inertial terms and using Hooke's law for the stress-strain relation, we obtain the stress equilibrium

$$0 = \frac{Y(1-\nu)}{(1+\nu)(1-2\nu)}\frac{\partial \varepsilon}{\partial x} - \alpha\frac{\partial p}{\partial x}. \tag{7a}$$

Young's modulus Y is often denoted E, but we abstain from this notation to avoid confusion with the elasticity E in compartment models. For ease of notation, we replace the quotient containing Poisson's ratio ν by

$$\nu_0 = \frac{(1-\nu)}{(1+\nu)(1-2\nu)}.$$

The saturation of the fluid is described by the Biot–Willis parameter α, a value of zero meaning that there is no fluid in the pores, hence the solid bears the whole load, a value of one meaning that the solid matrix is fully saturated with fluid, so the fluid bears the whole load. In brain tissue, we expect a value of α close to one, or possibly even larger than one, due to its more complex structure including nerve cells, CSF and blood vessels, which might react to pressure changes with autoregulation.

Defining the change in fluid content θ, as "the increment of water volume per unit volume of soil", Biot (1941) reaches a relation of the form

$$\theta = \alpha\varepsilon + s_e p. \tag{7b}$$

with another poroelastic constant s_e, the constraint specific storage coefficient. If the porous medium is compressed, that is ε becomes negative, but the pressure kept constant then fluid is forced out of the medium, θ becomes negative. If the pressure is increased, keeping the strain constant, then additional fluid is forced into the medium, so θ becomes positive.

The last governing equation is effectively Darcy flow through a porous medium, but with a strain-dependant permeability as proposed by Sobey and Wirth (2006)

$$\frac{\partial\theta}{\partial t} = \frac{\partial}{\partial x}\left(\frac{k_0}{\mu}e^{M\varepsilon}\frac{\partial p}{\partial x}\right) \tag{7c}$$

with a nonnegative constant M. Equations (7) define the system of partial differential equations, we need to solve for $(x,t) \in [0,L] \times [0,T]$.

4.2.2 Boundary Conditions

We consider boundary conditions similar to the ones assumed in the brain (Smillie et al., 2005). On the left end, the solid can move freely, so the combined stress in the porous medium has to balance the stress in the fluid adjacent to it

$$\nu_0 Y\varepsilon + \alpha p = -p \qquad (x = 0). \tag{8a}$$

Furthermore, we force a given flux $Q(t)$ into the system from the left end. This additional fluid will partly fill the space made available by moving the boundary of the porous medium and partly flow into the porous medium

$$-\frac{k_0}{\mu}\frac{\partial p}{\partial x}e^{M\frac{\partial u}{\partial x}} + \frac{\partial u}{\partial t} = Q(t) \qquad (x = 0). \tag{8b}$$

At the right boundary, the solid matrix will be fixed to a solid porous wall, so the fluid can leave freely into the surrounding space, where we prescribe the pressure p_s, but the solid matrix will not be displaced there.

$$p = p_s \qquad (x = L), \tag{8c}$$
$$u = 0 \qquad (x = L). \tag{8d}$$

The initial values will be taken to satisfy the steady state equation (see 4.3.1).

4.2.3 Pressure-Strain Formulation

The displacements u in their original form only appear in the boundary conditions, thus, we can eliminate them. Integrating ε and using the boundary condition (8d), we obtain

$$u(x,t) = -\int_x^L \varepsilon(s,t)\mathrm{d}s.$$

Inserting the definition of θ, we can turn the above problem into a system of only two unknowns

$$0 = \nu_0 Y \frac{\partial \varepsilon}{\partial x} - \alpha \frac{\partial p}{\partial x}, \tag{9a}$$

$$\alpha \frac{\partial \varepsilon}{\partial t} + s_e \frac{\partial p}{\partial t} = \frac{\partial}{\partial x}\left(\frac{k_0}{\mu} e^{M\varepsilon} \frac{\partial p}{\partial x}\right), \tag{9b}$$

with the (integral) boundary conditions

$$-\frac{k_0}{\mu}\frac{\partial p}{\partial x} e^{M\varepsilon} - \frac{\partial}{\partial t}\left(\int_x^L \varepsilon(s,t)\mathrm{d}s\right) = Q(t) \qquad (x=0), \tag{10a}$$

$$\nu_0 Y \varepsilon + (1-\alpha)p = 0 \qquad (x=0), \tag{10b}$$

$$p = p_s \qquad (x=L). \tag{10c}$$

The advantage of this formulation is that ε and p can be approximated by polynomials of the same order in the finite element approximation. The displacements can be obtained by simple analytic integration in the postprocessing.

4.2.4 Non-dimensionalisation

To consider the non-dimensionalised problem, let

$$\xi = \frac{x}{L} \qquad \tau = \frac{t}{T}$$

$$\bar{u}(\xi,\tau) = \frac{u(x,t)}{U} \qquad \bar{\varepsilon}(\xi,\tau) = \frac{L}{U}\varepsilon(x,t) \qquad \bar{p}(\xi,\tau) = \frac{p(x,t)}{P}$$

with U and P to be determined later on in (15). Then (9) and (10) become

$$0 = \frac{\partial \bar{\varepsilon}}{\partial \xi} - a_1 \frac{\partial \bar{p}}{\partial \xi} \tag{11a}$$

$$a_2 \frac{\partial \bar{\varepsilon}}{\partial \tau} + a_3 \frac{\partial \bar{p}}{\partial \tau} = a_4 \frac{\partial}{\partial \xi}\left(e^{\bar{M}\bar{\varepsilon}} \frac{\partial \bar{p}}{\partial \xi}\right) \tag{11b}$$

and

$$a_5 \frac{\partial \bar{p}}{\partial \bar{\xi}} e^{\bar{M}\bar{\varepsilon}} + \frac{\partial}{\partial \tau} \int_{\bar{\xi}}^{1} \bar{\varepsilon}(s,\tau)\mathrm{d}s = -\bar{Q}(\tau) \qquad (\bar{\xi} = 0) \tag{12a}$$

$$\bar{\varepsilon} + a_6 \bar{p} = 0 \qquad (\bar{\xi} = 0) \tag{12b}$$

$$\bar{p} = \bar{p}_s \qquad (\bar{\xi} = 1), \tag{12c}$$

respectively, with

$$a_1 = \alpha \frac{LP}{\nu_0 Y U}, \qquad a_2 = \alpha \frac{U}{L}, \qquad a_3 = s_e P,$$
$$a_4 = \frac{k_0 P T}{\mu L^2}, \qquad a_5 = \frac{k_0 P T}{\mu L U}, \qquad a_6 = (1-\alpha)\frac{LP}{\nu_0 Y U},$$
$$\bar{M} = M \frac{U}{L}, \qquad \bar{Q}(\tau) = \frac{T}{U} Q(\tau T), \qquad \bar{p}_s = \frac{p_s}{P}.$$

Using the parameter values given later in Table 4 on page 27 and a time scale of half an hour, we obtain

$$a_1 \sim 0.83, \qquad a_2 \sim 1.20, \qquad a_3 \sim 0.15,$$
$$a_4 \sim 0.05, \qquad a_5 \sim 0.03, \qquad a_6 \sim 0.17,$$
$$\bar{M} \sim 6.23, \qquad \bar{Q} \sim 0.03, \qquad \bar{p}_s = 0.$$

4.3 Steady State

4.3.1 Steady State Problem

As a first step, we consider the steady state. This is necessary, since we require our initial condition to be in steady state, and will furthermore give a basic understanding of the governing equations. Without time dependence, the system of partial differential equations (11)–(12) looks as follows

$$0 = \frac{\mathrm{d}\bar{\varepsilon}}{\mathrm{d}\bar{\xi}} - a_1 \frac{\mathrm{d}\bar{p}}{\mathrm{d}\bar{\xi}}, \tag{13a}$$

$$0 = \frac{\mathrm{d}}{\mathrm{d}\bar{\xi}} \left(e^{\bar{M}\bar{\varepsilon}} \frac{\mathrm{d}\bar{p}}{\mathrm{d}\bar{\xi}} \right), \tag{13b}$$

with the boundary conditions

$$-a_5 \frac{\mathrm{d}\bar{p}}{\mathrm{d}\bar{\xi}} e^{\bar{M}\bar{\varepsilon}} = \bar{Q} \qquad (\bar{\xi} = 0), \tag{14a}$$

$$\bar{\varepsilon} + a_6 \bar{p} = 0 \qquad (\bar{\xi} = 0), \tag{14b}$$

$$\bar{p} = \bar{p}_s \qquad (\bar{\xi} = 1). \tag{14c}$$

4.3.2 Steady State with Constant Permeability

For $M = 0$, that is with strain independent permeability, we obtain the linear system of differential equations

$$0 = \frac{\mathrm{d}\bar{\varepsilon}}{\mathrm{d}\xi} - a_1 \frac{\mathrm{d}\bar{p}}{\mathrm{d}\xi},$$
$$0 = \frac{\mathrm{d}^2\bar{p}}{\mathrm{d}\xi^2},$$

with boundary conditions

$$a_5 \frac{\mathrm{d}\bar{p}}{\mathrm{d}\xi} = -\bar{Q} \qquad (\xi = 0),$$
$$\bar{\varepsilon} + a_6 \bar{p} = 0 \qquad (\xi = 0),$$
$$\bar{p} = \bar{p}_s \qquad (\xi = 1),$$

yielding the solutions

$$\bar{p}(\xi) = \frac{\mu L Q}{k_0 P}\left[\left(1 + \frac{k_0 p_s}{\mu L Q}\right) - \xi\right]$$

and

$$\bar{\varepsilon}(\xi) = \frac{\mu L^2 Q}{\nu_0 k_0 Y U}\left[-\alpha\xi - (1-\alpha)\left(1 + \frac{k_0 p_s}{\mu L Q}\right)\right],$$

hence

$$\bar{u}(\xi) = \frac{\mu L^2 Q}{\nu_0 k_0 Y U}\left[-\frac{\alpha}{2}\xi^2 - (1-\alpha)\left(1 + \frac{k_0 p_s}{\mu L Q}\right)\xi + \left(1 - \frac{\alpha}{2}\right) + (1-\alpha)\frac{k_0 p_s}{\mu L Q}\right].$$

Before the infusion starts, the whole system is in steady state with $Q = Q_{\text{prod}}$. Hence, we choose the following values to non-dimensionalise p and ε

$$P = \frac{\mu}{k_0} L Q_{\text{prod}}, \qquad U = \frac{\mu L^2}{\nu_0 k_0 Y} Q_{\text{prod}}. \tag{15}$$

In the following subsections, we omit the bar on the non-dimensionalised functions, but will give results with dimensions in subsection 4.5.

4.3.3 Steady State with Variable Permeability

Even with strain dependent permeability, hence $M > 0$, we can find an analytic solution of (13). Inserting (13a) into (13b), we receive

$$\begin{aligned} 0 &= \frac{1}{a_1}\frac{\mathrm{d}}{\mathrm{d}\xi}\left(e^{\bar{M}\bar{\varepsilon}}\frac{\mathrm{d}\bar{\varepsilon}}{\mathrm{d}\xi}\right) = \frac{1}{a_1}\left(e^{\bar{M}\bar{\varepsilon}}\bar{M}\frac{\mathrm{d}\bar{\varepsilon}}{\mathrm{d}\xi}\frac{\mathrm{d}\bar{\varepsilon}}{\mathrm{d}\xi} + e^{\bar{M}\bar{\varepsilon}}\frac{\mathrm{d}^2\bar{\varepsilon}}{\mathrm{d}\xi^2}\right) \\ &= \frac{1}{a_1}e^{\bar{M}\bar{\varepsilon}}\left(\bar{M}\left(\bar{\varepsilon}'\right)^2 + \frac{\mathrm{d}}{\mathrm{d}\xi}\bar{\varepsilon}'\right), \end{aligned}$$

which is equivalent to

$$0 = \bar{M}\left(\bar{\varepsilon}'\right)^2 + \frac{\mathrm{d}}{\mathrm{d}\xi}\bar{\varepsilon}'.$$

This can be solved by a function of the form

$$\bar{\varepsilon}'(\xi) = \left(\bar{M}\xi - C_1\right)^{-1} = -\left(C_1 - \bar{M}\xi\right)^{-1},$$

where C_1 is a constant to be determined by the boundary conditions. Integrating once, we obtain

$$\bar{\varepsilon}(\xi) = \frac{1}{\bar{M}}\log\left|C_1 - \bar{M}\xi\right| + C_2,$$

and similarly from

$$\bar{p}'(\xi) = -\frac{1}{a_1}\left(C_1 - \bar{M}\xi\right)^{-1},$$

we obtain

$$\bar{p}(\xi) = \frac{1}{a_1\bar{M}}\log\left|C_1 - \bar{M}\xi\right| + C_3.$$

We expect positive flux from left to right in each point, hence, the pressure derivative needs to be negative everywhere, which requires that $C_1 > \bar{M} > 0$. From the boundary conditions (14) in reverse order, we receive

$$\begin{aligned} C_3 &= \bar{p}_s - \frac{1}{a_1\bar{M}}\log\left|C_1 - \bar{M}\right|, \\ C_2 &= -\left(1 + \frac{a_6}{a_1}\right)\frac{1}{\bar{M}}\log\left|C_1\right| - a_6\bar{p}_s + \frac{a_6}{a_1}\frac{1}{\bar{M}}\log\left|C_1 - \bar{M}\right|, \end{aligned}$$

and

$$\frac{1}{a_1}C_1^{-1}\exp\left(\log\left|C_1\right| + \bar{M}C_2\right) = \frac{\bar{Q}}{a_5}.$$

Inserting C_2, we obtain

$$C_1^{-1}|C_1| \exp\left(-\left(1+\frac{a_6}{a_1}\right)\log|C_1| - \bar{M}a_6\bar{p}_s + \frac{a_6}{a_1}\log|C_1-\bar{M}|\right) = \frac{a_1}{a_5}\bar{Q},$$

thus,

$$F(C_1) := C_1^{-\left(1+\frac{a_6}{a_1}\right)}(C_1-\bar{M})^{\frac{a_6}{a_1}} = |C_1|^{-\left(1+\frac{a_6}{a_1}\right)}|C_1-\bar{M}|^{\frac{a_6}{a_1}} = \frac{a_1}{a_5}\bar{Q}e^{\bar{M}a_6\bar{p}_s}.$$

We get $F(C_1) \to 0$ for $C_1 \to +\infty$, as well as for $C_1 \to M$. Differentiating F tells us, that $F(C_1)$ reaches its maximal value

$$F(C_1^\star) = \frac{\alpha}{\bar{M}}(1-\alpha)^{\frac{1-\alpha}{\alpha}}$$

at

$$C_1^\star = \left(1+\frac{a_6}{a_1}\right)\bar{M} = \left(1+\frac{1-\alpha}{\alpha}\right)\bar{M} = \frac{\bar{M}}{\alpha},$$

which gives us a test of solvability of the problem (13)-(14) for given parameter values, that is for positive $\bar{Q}$, there is a solution if and only if

$$\frac{a_1}{a_5}\bar{Q}e^{\bar{M}a_6\bar{p}_s} \leq \frac{\bar{M}}{\alpha}. \tag{16}$$

A similar derivation can also be found in the appendix of Wirth (2005).

Doing the same analysis for negative flux, we get the requirement $C_1 < 0$ and from the boundary condition (14a), we obtain

$$G(C_1) := (-C1)^{\left(1+\frac{a_6}{a_1}\right)}(\bar{M}-C1)^{\frac{a_6}{a_1}} = -\frac{a_1}{a_5}\bar{Q}e^{a_6\bar{M}p_s}.$$

Both, the right hand side and the left hand side of this equation are positive and the image of $[-\infty, 0)$ under G is $(0, \infty)$, so for negative flux, the differential equation always has a solution.

For $|C_1| \to \infty$, both cases converge to the same constant solution. Hence, we consider all quantities as functions of $\frac{1}{C_1}$, where $-\infty < \frac{1}{C_1} < \frac{1}{\bar{M}}$. Another requirement we need to fulfil is $\varepsilon > -1$, that is $\bar{\varepsilon} > -\frac{L}{U}$. Otherwise, the small strain model breaks down because matter would penetrate itself, which is of course unphysical. We only need to consider the case of Q being positive, the smallest strain then being at $\xi = 1$. Inserting all the formulae, we end up with the claim

$$-\infty < \frac{1}{C_1} < \frac{1}{\bar{M}}\left(1-\exp\left(\alpha\bar{M}\left(a_6\bar{p}_s - \frac{L}{U}\right)\right)\right). \tag{17}$$

In the following figures, the upper bound for $1/C_1$ is $1/\bar{M} \approx 8.24$ and $1/C_1^\star \approx 6.84$. In Figures 2(a) and 2(b), we plot the flux and the pressure at the left end as functions of $1/C_1$. In Figure 3, we eliminate $1/C_1$ and plot the flux Q versus the pressure $p_0 = p(0)$. As the pressure is increased, the flux only increases up to a certain maximum and finally decreases towards 0, as $p_0 \to \infty$. In "real life", with a given flux, we would rather expect solutions, where the pressure is smaller than the pressure for maximal flux. Figure 4 shows examples of the strain distribution through the porous medium for different values of $1/C_1$.

4.4 Finite Element Approach

So far, we have only implemented the steady state equation (13). To consider its weak form, that is for ε and p in $H^1([0,1])$, first multiply (13a) with a test function $\varphi \in H^1([0,1])$, integrate and use the divergence theorem to obtain

$$0 = \int_0^1 \left(\varepsilon' - a_1 p'\right) \varphi \mathrm{d}\xi = -\int_0^1 \left(\varepsilon - a_1 p\right) \varphi' \mathrm{d}\xi + \left[\left(\varepsilon - a_1 p\right) \varphi\right]_0^1.$$

Since we have three instead of four boundary conditions, using only test functions in $H_0^1([0,1])$ would lead to an underdetermined system of equations in the finite element version. Note that the boundary term is well defined due to the continuity of ε, p and φ. For the second equation, we can restrict φ to $H_0^1([0,1])$ and obtain

$$0 = \int_0^1 \frac{\mathrm{d}}{\mathrm{d}\xi}\left(e^{M\varepsilon} p'\right) \varphi \mathrm{d}\xi = -\int_0^1 e^{M\varepsilon} p' \varphi' \mathrm{d}\xi.$$

Knowing this, we can define

$$A\left(\begin{pmatrix}\varepsilon\\ p\end{pmatrix}, \varphi\right) := \int_0^1 \left(\varepsilon - a_1 p\right) \varphi' \mathrm{d}\xi - \left[\left(\varepsilon - a_1 p\right) \varphi\right]_0^1,$$
$$B\left(\begin{pmatrix}\varepsilon\\ p\end{pmatrix}, \varphi\right) := \int_0^1 e^{M\varepsilon} p' \varphi' \mathrm{d}\xi$$

and obtain the weak formulation of (13) as: Find $\varepsilon, p \in H^1([0,1])$, such that

$$A\left(\begin{pmatrix}\varepsilon\\ p\end{pmatrix}, \varphi\right) = 0 \qquad \forall \varphi \in H^1([0,1]), \tag{18a}$$
$$B\left(\begin{pmatrix}\varepsilon\\ p\end{pmatrix}, \varphi\right) = 0 \qquad \forall \varphi \in H_0^1([0,1]). \tag{18b}$$

This is a nonlinear system of equations, so we use Newton's method to solve it, which requires the linearisation of A and B with respect to $(\varepsilon, p)^T$. Let

$$\|\Delta\varepsilon\|_{H^1([0,1])} = \mathcal{O}(\delta) \qquad \|\Delta p\|_{H^1([0,1])} = \mathcal{O}(\delta)$$

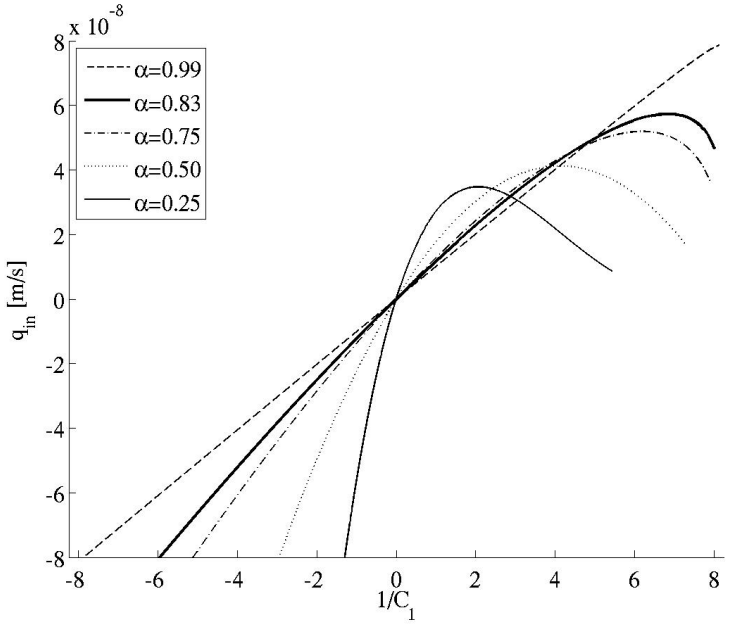

(a) Flux Q over $1/C_1$ for different values of α

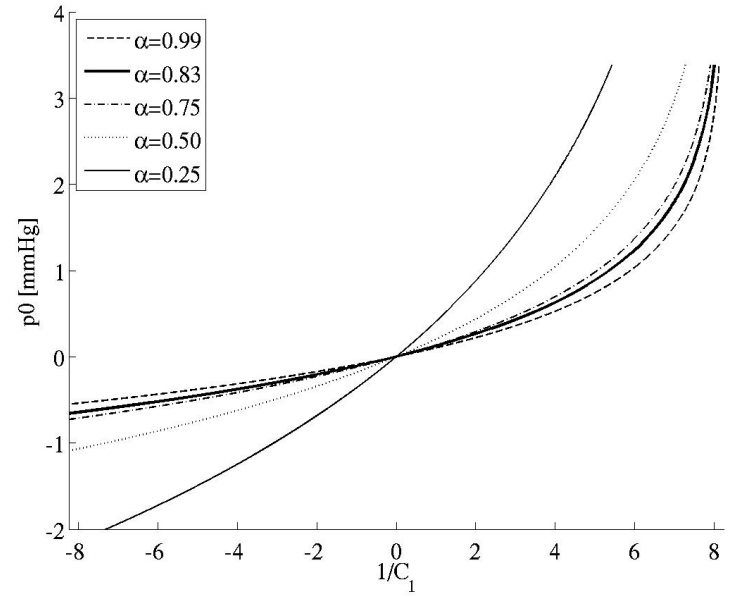

(b) Pressure p_0 at $\xi = 0$ over $1/C_1$ for different values of α

Fig. 2: Pressure and flux at the left boundary as functions of $1/C_1$

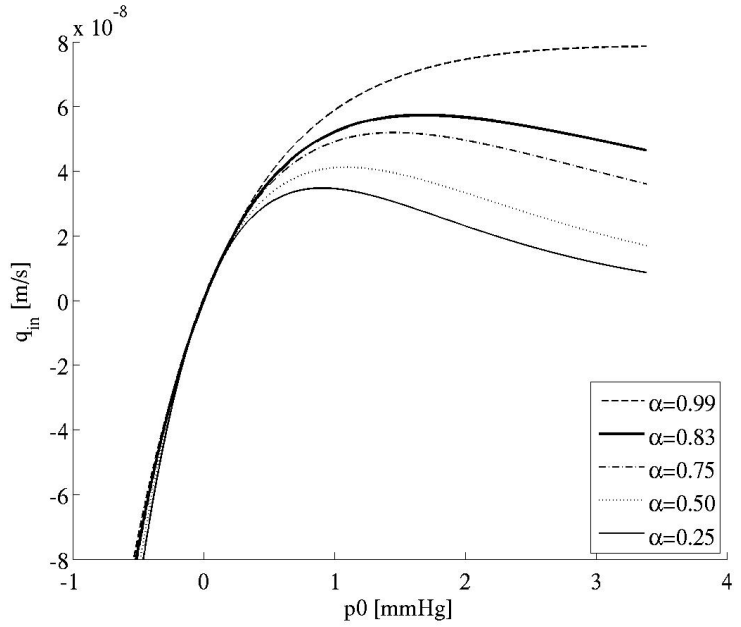

Fig. 3: Flux Q over pressure p_0 for different values of α

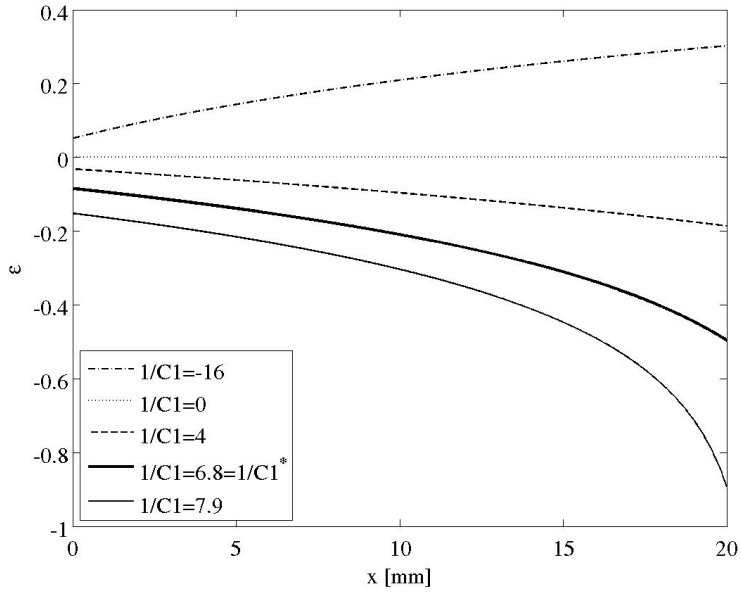

Fig. 4: Strain $\varepsilon(x)$ for different values of $1/C_1$

and consider

$$\begin{aligned}
A\left(\begin{pmatrix}\varepsilon+\Delta\varepsilon\\ p+\Delta p\end{pmatrix},\varphi\right) &= \int_0^1 (\varepsilon+\Delta\varepsilon-a_1p-a_1\Delta p)\,\varphi'\mathrm{d}\xi - \left[(\varepsilon+\Delta\varepsilon-a_1p-a_1\Delta p)\,\varphi\right]_0^1\\
&= A\left(\begin{pmatrix}\varepsilon\\ p\end{pmatrix},\varphi\right) + A\left(\begin{pmatrix}\Delta\varepsilon\\ \Delta p\end{pmatrix},\varphi\right),\\
B\left(\begin{pmatrix}\varepsilon+\Delta\varepsilon\\ p+\Delta p\end{pmatrix},\varphi\right) &= \int_0^1 e^{M\varepsilon}e^{M\Delta\varepsilon}(p'+\Delta p')\varphi'\mathrm{d}\xi\\
&= \int_0^1 e^{M\varepsilon}\left(1+M\Delta\varepsilon+\dots\right)(p'+\Delta p')\varphi'\mathrm{d}\xi\\
&= B\left(\begin{pmatrix}\varepsilon\\ p\end{pmatrix},\varphi\right) + B\left(\begin{pmatrix}\varepsilon\\ \Delta p\end{pmatrix},\varphi\right) + M\int_0^1 e^{M\varepsilon}\Delta\varepsilon p'\varphi'\mathrm{d}\xi + \mathcal{O}(\delta^2).
\end{aligned}$$

Hence the linearisations are

$$\mathcal{D}A\left(\begin{pmatrix}\varepsilon\\ p\end{pmatrix};\begin{pmatrix}\Delta\varepsilon\\ \Delta p\end{pmatrix},\varphi\right) = A\left(\begin{pmatrix}\Delta\varepsilon\\ \Delta p\end{pmatrix},\varphi\right)$$

and

$$\mathcal{D}B\left(\begin{pmatrix}\varepsilon\\ p\end{pmatrix};\begin{pmatrix}\Delta\varepsilon\\ \Delta p\end{pmatrix},\varphi\right) = B\left(\begin{pmatrix}\varepsilon\\ \Delta p\end{pmatrix},\varphi\right) + M\int_0^1 e^{M\varepsilon}\Delta\varepsilon p'\varphi'\mathrm{d}\xi.$$

Similarly, we define the vector of boundary conditions from (14)

$$C\left(\begin{pmatrix}\varepsilon\\ p\end{pmatrix}\right) := \begin{pmatrix}a_5p'(0)e^{M\varepsilon(0)}+Q\\ \varepsilon(0)+a_6p(0)\\ p(1)-p_s\end{pmatrix}$$

and receive the linearisation

$$\mathcal{D}C\left(\begin{pmatrix}\varepsilon\\ p\end{pmatrix};\begin{pmatrix}\Delta\varepsilon\\ \Delta p\end{pmatrix}\right) = \begin{pmatrix}a_5e^{M\varepsilon(0)}\left[\Delta p'(0)+Mp'(0)\Delta\varepsilon(0)\right]\\ \Delta\varepsilon(0)+a_6\Delta p(0)\\ \Delta p(1)\end{pmatrix}.$$

Here, we actually have to be a bit more careful to define $p'(0)$ and $\Delta p'(0)$ as the limit from inside the interval, since the weak derivatives need not be continuous. In practice this does not cause any trouble, since we only consider the functions inside the interval. Substituting the first boundary condition with a pressure boundary condition is of course easy and makes the problem well posed.

For the Finite element formulation, choose nodes $0 = \xi_0 < \xi_1 < \cdots < \xi_{N-1} < \xi_N = 1$ and let $h_k := \xi_k - \xi_{k-1}$. For $k = 0, \ldots, N$, define the piecewise linear base functions

$$\varphi_k(\xi) := \begin{cases} \frac{\xi - \xi_{k-1}}{h_k} & (\xi_{k-1} \le \xi \le \xi_k), \\ \frac{\xi_{k+1} - \xi}{h_{k+1}} & (\xi_k < \xi \le \xi_{k+1}), \\ 0 & (\text{otherwise}), \end{cases}$$

with their weak derivatives

$$\varphi_k'(\xi) := \begin{cases} \frac{1}{h_k} & (\xi_k \le \xi < \xi_k), \\ -\frac{1}{h_{k+1}} & (\xi_k < \xi \le \xi_{k+1}), \\ 0 & (\text{otherwise}). \end{cases}$$

The finite element version of (13)-(14) is then: Find $\epsilon, \mathrm{p} \in \mathbb{R}^{N+1}$, such that with

$$\hat{\varepsilon} = \sum_{k=-1}^{N} \epsilon_k \varphi_k, \qquad \hat{p} = \sum_{k=0}^{N} \mathrm{p}_k \varphi_k$$

the following $2N + 2$ equations are satisfied

$$A\left(\begin{pmatrix} \hat{\varepsilon} \\ \hat{p} \end{pmatrix}, \varphi_j\right) = 0 \qquad (j = 1, \ldots, N), \tag{19a}$$

$$B\left(\begin{pmatrix} \hat{\varepsilon} \\ \hat{p} \end{pmatrix}, \varphi_j\right) = 0 \qquad (j = 1, \ldots, N-1), \tag{19b}$$

$$C\left(\begin{pmatrix} \hat{\varepsilon} \\ \hat{p} \end{pmatrix}\right) = 0. \tag{19c}$$

Since we have one boundary condition less at $\xi = 1$, we chose the additional equation at this boundary, that is for $j = N$.

So in each iteration, the Newton step $(\Delta\epsilon, \Delta\mathrm{p})^T \in \mathbb{R}^{2N+2}$ needs to satisfy

$$\mathcal{D}A\left(\begin{pmatrix} \hat{\varepsilon} \\ \hat{p} \end{pmatrix}; \begin{pmatrix} \Delta\hat{\varepsilon} \\ \Delta\hat{p} \end{pmatrix}, \varphi_j\right) = -A\left(\begin{pmatrix} \hat{\varepsilon} \\ \hat{p} \end{pmatrix}, \varphi_j\right) \qquad (j = 1, \ldots, N), \tag{20a}$$

$$\mathcal{D}B\left(\begin{pmatrix} \hat{\varepsilon} \\ \hat{p} \end{pmatrix}; \begin{pmatrix} \Delta\hat{\varepsilon} \\ \Delta\hat{p} \end{pmatrix}, \varphi_j\right) = -B\left(\begin{pmatrix} \hat{\varepsilon} \\ \hat{p} \end{pmatrix}, \varphi_j\right) \qquad (j = 1, \ldots, N-1), \tag{20b}$$

$$\mathcal{D}C\left(\begin{pmatrix} \hat{\varepsilon} \\ \hat{p} \end{pmatrix}; \begin{pmatrix} \Delta\hat{\varepsilon} \\ \Delta\hat{p} \end{pmatrix}\right) = -C\left(\begin{pmatrix} \hat{\varepsilon} \\ \hat{p} \end{pmatrix}\right). \tag{20c}$$

More details of the implementation of this linear system of equations are given in appendix A.3.

Newton's method does not necessarily converge for all starting points. A damped Newton approach reduces the overshoot in the beginning and can lead to much bet-

Thickness of porous medium	L	=	$70\text{ mm} = 7 \cdot 10^{-2}\text{ m}$
Shear modulus	G	=	$216\text{ Pa} \approx 1.62\text{ mmHg}$
Poisson's ratio	ν	=	0.35
Young's modulus	Y	=	$2G(1-\nu) \approx 2.11\text{ mmHg}$
(one) Lamé constant	λ	=	$524\text{ Pa} \approx 3.94\text{ mmHg}$
bulk modulus (of solid)	K	=	$\lambda + \frac{2G}{3} \approx 5.02\text{ mmHg}$
Biot-Willis parameter	α	=	0.83
Skempton's coefficient	β	=	0.99
constraint specific storage coeff.	s_e	=	$\frac{(1-\alpha\beta)\alpha}{K\beta} \approx 2.98 \cdot 10^{-2} \frac{1}{\text{mmHg}}$
permeability	k_0	=	$1.4 \cdot 10^{-14}\text{ m}^2$
viscosity	μ	=	$8.9 \cdot 10^{-4}\text{ Pa s} \approx 6.69 \cdot 10^{-6}\text{ mmHg s}$
area CSF production rate	Q_{prod}	=	$\frac{5.8 \cdot 10^{-9} \frac{\text{m}^3}{\text{s}}}{4\pi(30\text{ mm})^2} \approx 5.13 \cdot 10^{-7} \frac{\text{m}}{\text{s}}$
area infusion rate	Q_{inf}	=	$\frac{1.5 \cdot \frac{\text{ml}}{\text{min}}}{4\pi(30\text{ mm})^2} \approx 2.21 \cdot 10^{-6} \frac{\text{m}}{\text{s}}$
sagittal sinus pressure	p_s	=	0 mmHg
model parameter	M	=	4.3

Table 4: Standard parameter values

ter results. Instead of adding the whole step, we set

$$\begin{pmatrix} \epsilon \\ \text{p} \end{pmatrix}^{(j+1)} = \begin{pmatrix} \epsilon \\ \text{p} \end{pmatrix}^{(j)} + \left(1 - \omega^j\right) \begin{pmatrix} \Delta\epsilon \\ \Delta\text{p} \end{pmatrix}^{(j)}$$

with a damping parameter $\omega \in [0, 1)$. In this way, the steps are smaller in the beginning but converge to full Newton steps at later iterations as $\omega^j \to 0$. No damping is applied for $\omega = 0$.

4.5 Numerical Results

Almost all parameter values (Table 4) were taken from Wirth and Sobey (2006). The CSF production and infusion rates were divided by the approximate surface area of the ventricles to transform them into flow rates per area, hence fluxes. Since with these values, the solvability condition (16) does hot hold, we reduced the given flux at the left boundary to $Q = 5 \cdot 10^{-8} \frac{\text{m}}{\text{s}}$.

Figure 5 shows the pressure of the finite element solution and intermediate iterations of this problem with $N + 1 = 251$ equidistant nodes. Without damping, seven iterations and less than four seconds were necessary, until the relative size of the Newton step drops below the required tolerance of 10^{-12}.

The quadratic convergence of Newton's method close to the solution is clearly visible. The relative sizes in the l^2-norm of both, the last Newton step and the error to the analytic solution, are of the order 10^{-15}. Since the flow rate is constant throughout the

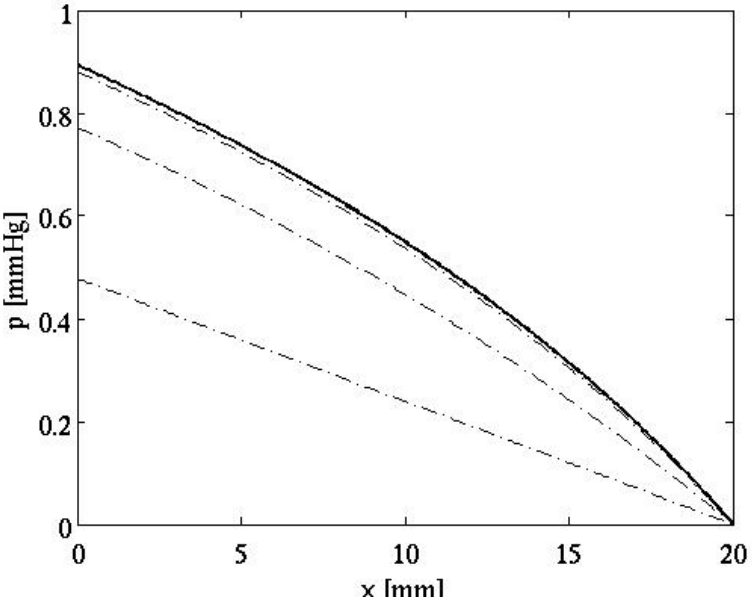

Fig. 5: Intermediate (···) and final (—) iterations of the pressure through the medium for given flux with $N = 250$ and no damping

whole medium, the decrease in permeability (Figure 6) towards the right end is the limiting factor for the flow rate.

To test the implementation further, we have also computed examples with a given pressure instead of the prescribed flux at the left end. Using the same parameters as above ($N = 250, \text{tol} = 10^{-12}$, no damping) the problem with boundary condition $p(0) = 5\text{mmHg}$ needs 18 iterations and 8.7 seconds. Looking more closely at the iterations in Figure 7, we see that in the first step, the linear problem without strain dependence in the permeability is solved, producing the straight line below the final solution. The next step after this overshoots the real solution by far, giving the highest curve. Afterwards, the real solution is approached in a linear fashion until the region of quadratic convergence is reached in the fourteenth iteration. Using appropriate damping, in this case $\omega \approx 0.25$, the overshoot can be avoided to a great extent, halving the number of iterations and reducing the computation time to 4.5 seconds (Figure 8).

It seems as if the optimal damping parameter does not depend on the number of elements. The same behaviour is observed for all tested cases (N=8, 250, 1024). This means that it can be estimated experimentally with few elements and a higher tolerance before starting the simulation with the required number of elements and nodes. For example with $p(0) = 15\text{mmHg}$, a damping of $\omega \leq 0.99$ leads to singular matrices, whereas with $\omega = 0.999$, the size of the Newton step drops below 10^{-10} after 210 iterations, for N=8 as well as for N=1024.

In this case, though, the relative error is of the order $5 \cdot 10^{-7}$. This is due to the large gradient at the right end, which cannot be resolved properly. When the nodes are dis-

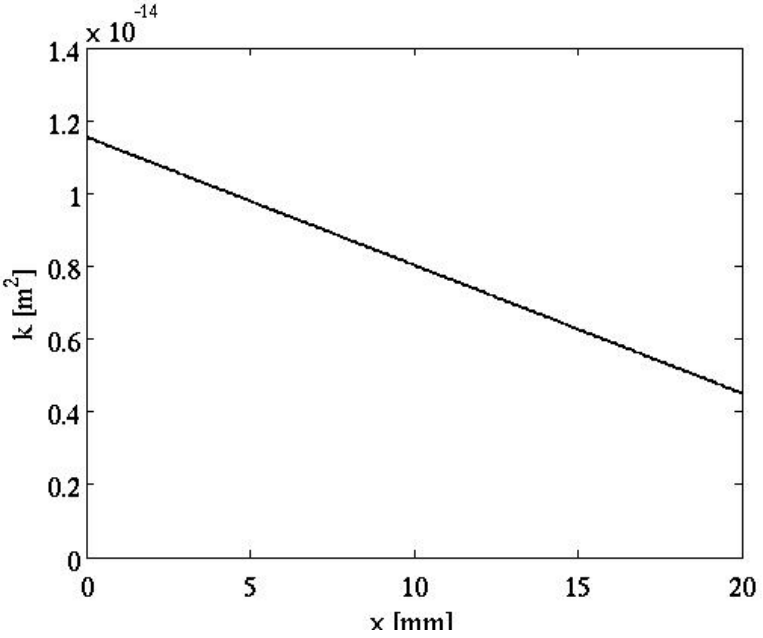

Fig. 6: Permeability distribution through the medium for given flux with $N = 250$ and no damping

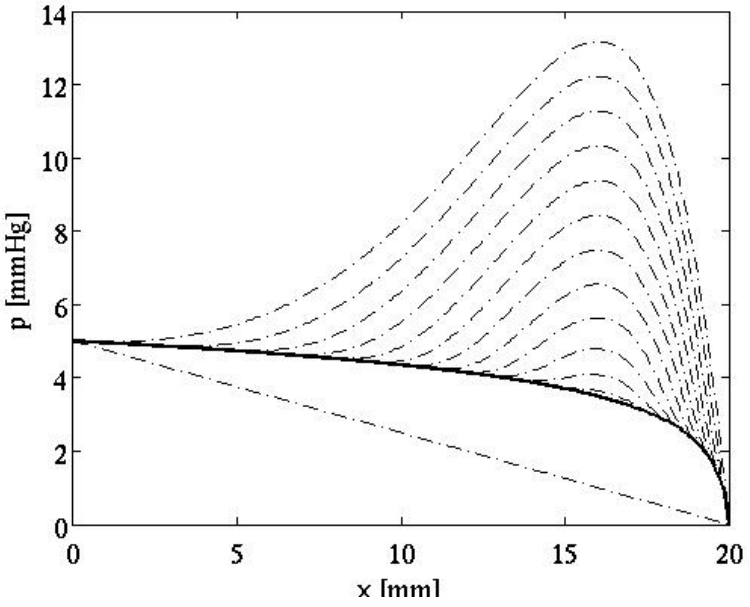

Fig. 7: Intermediate (-··-) and final (—) iterations of the pressure through the medium for given pressure $p(0) = 5$mmHg with $N = 250$ and no damping

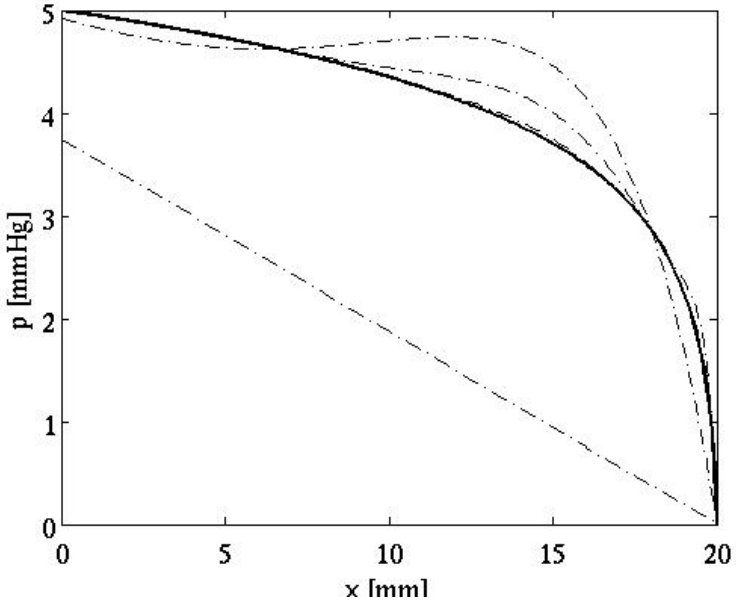

Fig. 8: Intermediate (-··-) and final (—) iterations of the pressure through the medium for given pressure $p(0) = 5$mmHg with $N = 250$ and damping $\omega = 0.25$

tributed in the interval like Chebyshev points in [-1,1], that is clustered towards the boundaries, though, the relative error size stays of the order of the tolerance in all tested cases. Furthermore, problems with large pressure gradients cannot be modelled with linear elasticity, since already for pressures above 3.4 mmHg at the left boundary, the predictions become unphysical with $\varepsilon < -1$. So, we expect to be able to simulate time dependent problems with reasonable boundary conditions with this approach to sufficient accuracy as well.

5 Further Research

Our overall aim is to be able to simulate the infusion test with a biomechanical model using the theory of poroelasticity. Hence, we need to build up the current model and finite element implementation. The next step is naturally to include and examine time dependence in the one-dimensional problem (11). We plan to do this with a suitable ODE solver already implemented in MATLAB (such as `ode45`). Especially the behaviour for oscillatory problems with a pressure dependent outflow as in the compartment models will be of interest. In this case, inertial terms might be of greater influence, so that they might need to be included.

The major extension will be to a spherically symmetric model derived in Wirth and Sobey (2006), but solved there with a finite difference method that only poorly resolves

layers near the boundaries. Such layers are easily seen in Figure 8 near the right hand boundary. In addition, the boundary conditions will be adapted to account for the aqueduct connecting the ventricles and the subarachnoid space.

The following changes in the governing equations should preferably be implemented and examined for the one-dimensional and the spherically symmetric model simultaneously. In a hydrocephalic brain, the deformations can be large, so a small strain approximation might limit the results too much. Thus, we want to include the influence of nonlinear elasticity and possibly also viscoelastic effects of the solid in the simulation. Due to the strain dependent permeability, we are already solving a nonlinear system of ordinary differential equations. So, the computational effort should not increase by too much.

As proposed in Wirth and Sobey (2009), we want to include arterial blood in addition to brain tissue and CSF in a triphasic poroelastic approach, possibly even extending it to a tetraphasic model with both arterial and venous blood. Furthermore, the permeability model needs to be revised. In the current exponential form, no choking can occur, that is even if the porous medium has been compressed to the extent that all the fluid must have been squeezed out, the current model would still predict some fluid flow through the medium.

Moreover, the results of (Löfgren and Zwetnow, 1973) as well as image reconstructions by Linninger et al. (2007, 2009a) indicate that the oscillatory CSF flow into the spinal cavity is by far not negligible, so we also need to find a suitable way of representing this in our model. When a set of governing equations is found that yields sufficiently good qualitative results, then this could be implemented in more realistic geometries. Nevertheless, quantitatively accurate results can only be expected with better knowledge of the material parameters and their spatial variation in the brain.

References

Andersson, N., Malm, J., and Eklund, A. (2008). Dependency of cerebrospinal fluid outflow resistance om intracranial pressure. *J. Neurosurg*, 109:918–922.

Biot, M. (1941). General theory of three dimensional consolidation. *Journal of Applied Physics*, 12:55–164.

Cheng, S., Clarke, E. C., and Bilston, L. E. (2008). Rheological properties of the tissue of the central nervous system: A review. *Medical Engineering & Physics*, 30:1318–1337.

Cirovic, S., Walsh, C., and Fraser, W. D. (2003). Mathematical study of the role of nonlinear venous compliance in the cranial volume-pressure test. *Medical & Biological Engineering & Computing*, 41:579–588.

Coussy, O. (2004). *Poromechanics*. John Wiley & Sons.

Czosnyka, M., Czosnyka, Z., Momjian, S., and Pickard, J. (2004). Cerebrospinal fluid dynamics. *Physiological Measurement*, 25:R51–R76.

Egnor, M., Rosiello, A., and Zheng, L. (2001). A model of intracranial pulsations. *Pediatr Neurosurg*, 35:284–298.

Egnor, M., Zheng, L., Rosiello, A., Gutman, F., and Davis, R. (2002). A model of pulsations in communicating hydrocephalus. *Pediatr Neurosurg*, 36:281–303.

Ehlers, W. and Markert, B. (2000). On the viscoelastic behaviour of fluid-saturated porous materials. *Granular Matter*, 2:153–161.

Guinane, J. E. (1972). An equivalent circuit analysis of cerebrospinal fluid hydrodynamics. *American Journal of Physiology*, 223(2):425–430.

Hakim, S., Venegas, J.-G., and Burton, J. (1976). The physics of the cranial cavity, hydrocephalus, and normal pressure hydrocephalus: Mechanical interpretation and mathmatical model. *Surgical Neurology*, 5:187–210.

Juniewicz, H., Kasprowicz, M., Czosnyka, M., Czosnyka, Z., Gizewski, S., Dzik, M., and Pickard, J. D. (2005). Analysis of intracranial pressure during and after the infusion test in patients with communicating hydrocephalus. *Physiological Measurement*, 26:1039–1048.

Kaczmarek, M., Subramaniam, R., and Neff, S. (1997). The hydromechanics of hydrocephalus: Steady state solution for cylindrical geometry. *Bulletin of Mathematical Biology*, 59:295–323.

Kellie, G. (1824). An account..., with some reflections on the pathology of the brain. *Transactions - Medicochirurgical Society of Edinburgh*, 1:84–169.

Levine, D. (1999). The pathogenesis of normal pressure hydrocephalus. *Bulletin of Mathematical Biology*, 61:875–916.

Levine, D. N. (2008). Intracranial pressure and ventricular expansion in hydrocephalus: Have we been asking the wrong question? *Journal of the Neurological Sciences*, 269:1–11.

Linninger, A. A., Sweetman, B., and Penn, R. (2009a). Normal and Hydrocephalic Brain Dynamics: The Role of Reduced Cerebrospinal Fluid Reabsorbtion in Ventricular Enlargement. *Annals of Biomedical Engineering*, 37(7):1434–1447.

Linninger, A. A., Tsakiris, C., Zhu, D. C., Xenos, M., Roycewicz, P., Danziger, Z., and Penn, R. (2005). Pulsatile Cerebrospinal Fluid Dynamics in the Human Brain. *IEE Transactions on biomedical engineering*, 52(4):557–565.

Linninger, A. A., Xenos, M., Sweetman, B., Ponkshe, S., Guo, X., and Penn, R. (2009b). A mathematical model of blood, cerebrospinal fluid and brain dynamics. *Journal of Mathematical Biology*, 59:729–759.

Linninger, A. A., Xenos, M., Zhu, D. C., Somayaji, M. R., Kondapalli, S., and Penn, R. D. (2007). Cerebrospinal Fluid Flow in the Normal and Hydrocephalic Human Brain. *IEEE Transactions on Biomedical Engineering*, 54(2):291–302.

Löfgren, J. and Zwetnow, N. N. (1973). Cranial and spinal components of the cerebrospinal fluid pressure-volume curve. *Acta Neurologica Scandinavica*, 49:575–585.

Marmarou, A., Shulman, K., and Rosende, R. M. (1978). A nonlinear analysis of the cerebrospinal fluid system and intracranial pressure dynamics. *J Neurosurg*, 48(3):332–344.

Miller, K. (1998). Modelling Soft Tissue Using Biphasic Theory – A Word of Caution. *Computer Methods in Biomechanis and Biomedical Engineering*, 1(3):261–263.

Miller, K. (1999). Constitutive model of brain tissue for finite element analysis of surgical procedures. *Journal of Biomechanics*, 32:475–479.

Monro, A. (1783). *Observations on the structure and functions of the nervous system. : Illustrated with tables*. Edinburgh : Printed for, and sold by, William Creech; and Joseph Johnson, ... London., M DCC LXXXIII.

Nagashima, T., Tamaki, N., Matsumoto, S., Horwitz, B., and Seguchi, Y. (1987). Biomechanics of hydrocephalus: A new theoretical model. *Neurosurgery*, 21:898–904.

Nolte, J. (2002). *The Human Brain: An Introduction to its Functional Anatomy*. St Louis, Mosby.

Sivaloganathan, S., Stastna, M., Tenti, G., and Drake, J. (2005a). A viscoelastic approach to the modelling of hydrocephalus. *Applied Mathematics and Computation*, 163:1097–1107.

Sivaloganathan, S., Stastna, M., Tenti, G., and Drake, J. (2005b). A viscoelastic model of the brain parenchyma with pulsatile ventricular pressure. *Applied Mathematics and Computation*, 165:687–698.

Smillie, A., Sobey, I., and Molnar, Z. (2005). A hydroelastic model of hydrocephalus. *Journal of Fluid Mechanics*, 539:417–443.

Sobey, I. and Wirth, B. (2006). Effect of non-linear permeability in a spherically symmetric model of hydrocephalus. *Mathematical Medicine and Biology*, 23:339–361.

Taylor, Z. and Miller, K. (2004). Reassessment of brain elasticity for analysis of biomechanisms of hydrocephalus. *Journal of Biomechanics*, 37:1263–1269.

Tenti, G., Drake, J., and Sivaloganathan, S. (2000). Brain biomechanics: Mathematical modelling of hydrocephalus. *Neurological Research*, 22:19–24.

Wang, H. F. (2000). *Theory of Linear Poroelasticity with Applications to Geomechanics and Hydrogeology*. Princeton University Press, 3 Market Place, Woodstock, Oxfordshire OX20 1SY.

Wirth, B. (2005). A mathematical model for hydrocephalus. Master's thesis, Oxford University.

Wirth, B. and Sobey, I. (2006). An axisymmetric and fully 3d poroelastic model for the evolution of hydrocephalus. *Mathematical Medicine and Biology*, 23:363–388.

Wirth, B. and Sobey, I. (2008). A model for an inverse power constitutive law for cerebral compliance. *Mathematical Medicine and Biology*, 25:113–131.

Wirth, B. and Sobey, I. (2009). Analytic solution during an infusion test of the linear unsteady poroelastic equations in a spherically symmetric model of the brain. *Mathematical Medicine and Biology*, 26(1):25–61.

A Appendix

A.1 Plots of Least Squares Fits

This appendix contains the plots corresponding to §3.4 on page 12.

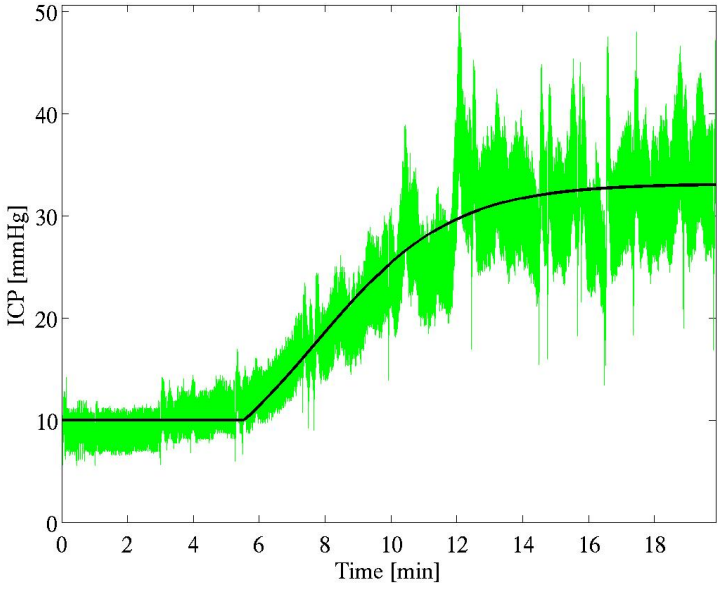

(a) Measured and fitted ICP

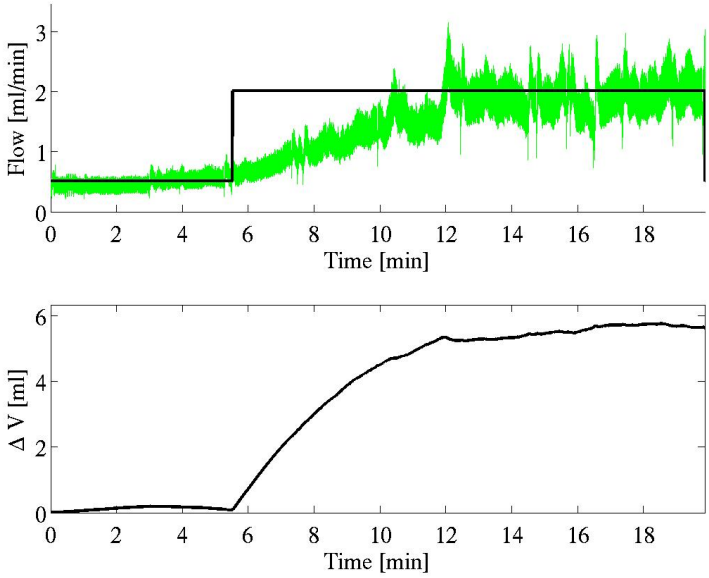

(b) Fluid Balance

Fig. 9: Plots for data set 00 version 1

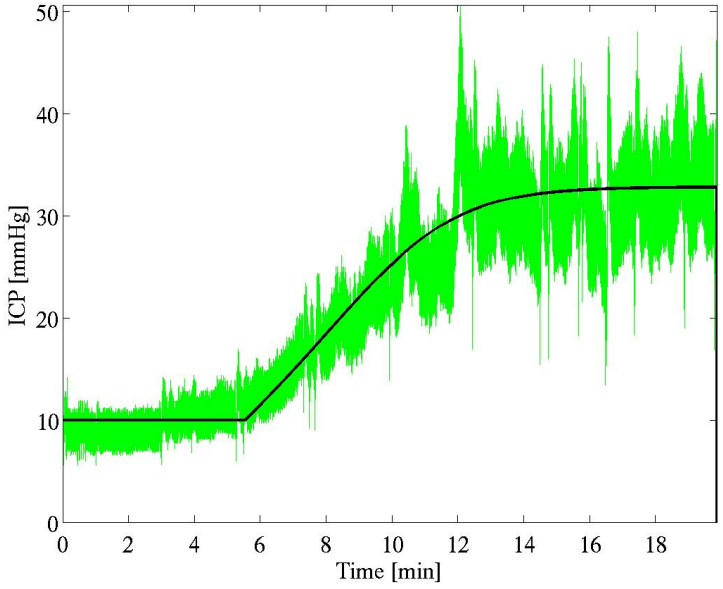

(a) Measured and fitted ICP

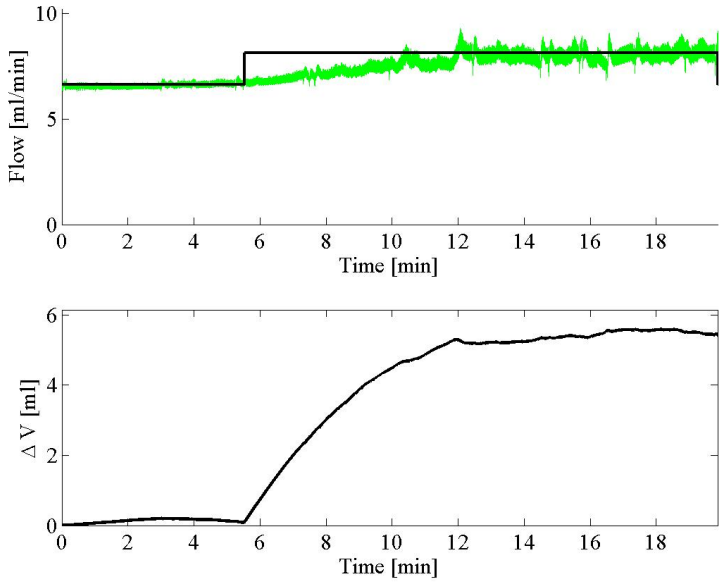

(b) Fluid Balance

Fig. 10: Plots for data set 00 version 2

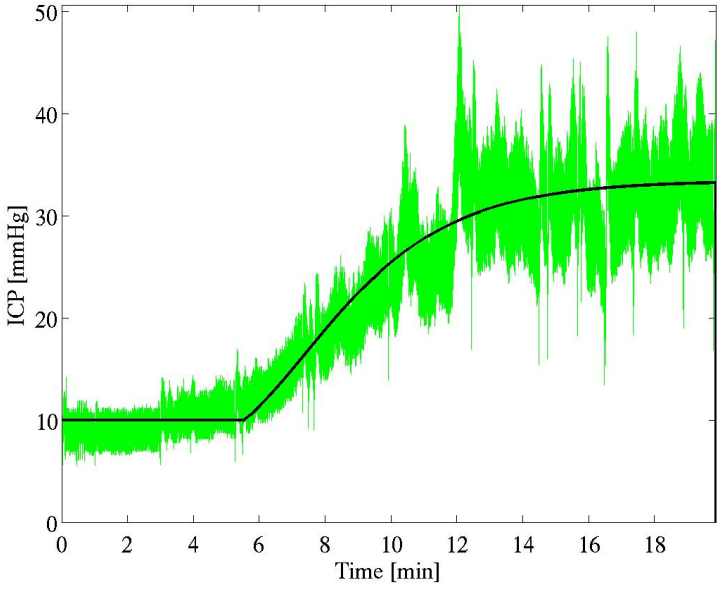

(a) Measured and fitted ICP

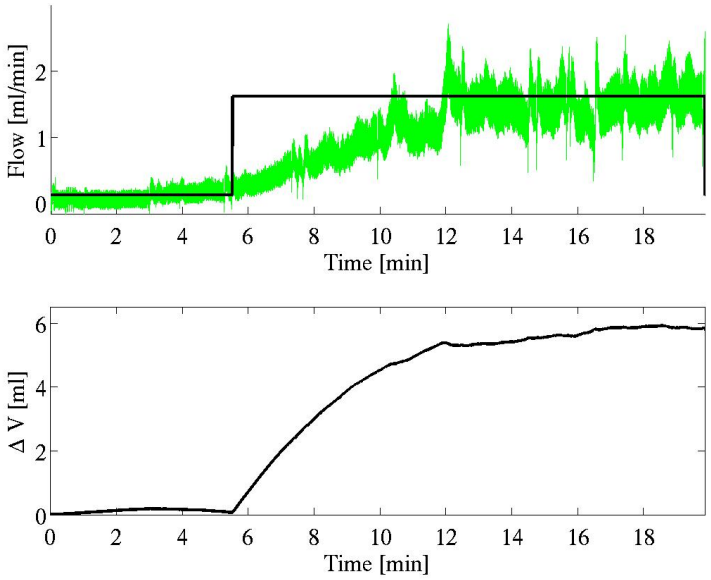

(b) Fluid Balance

Fig. 11: Plots for data set 00 version 3

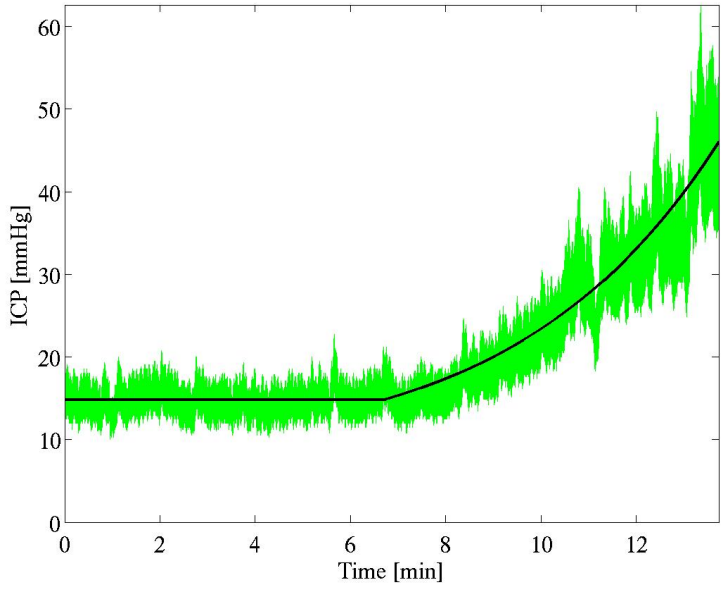

(a) Measured and fitted ICP

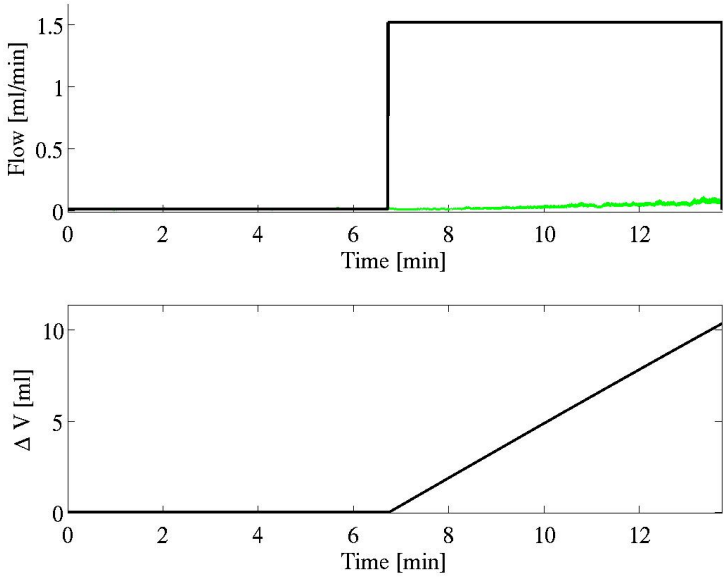

(b) Fluid Balance

Fig. 12: Plots for data set 01 version 1

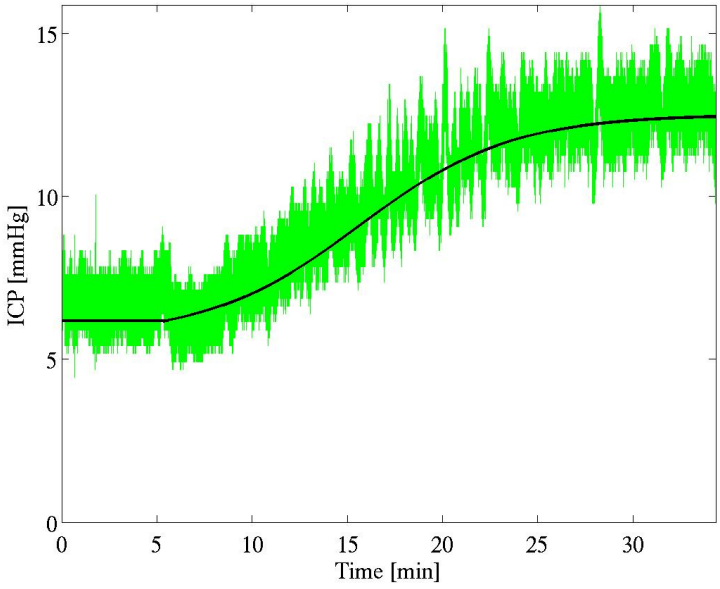

(a) Measured and fitted ICP

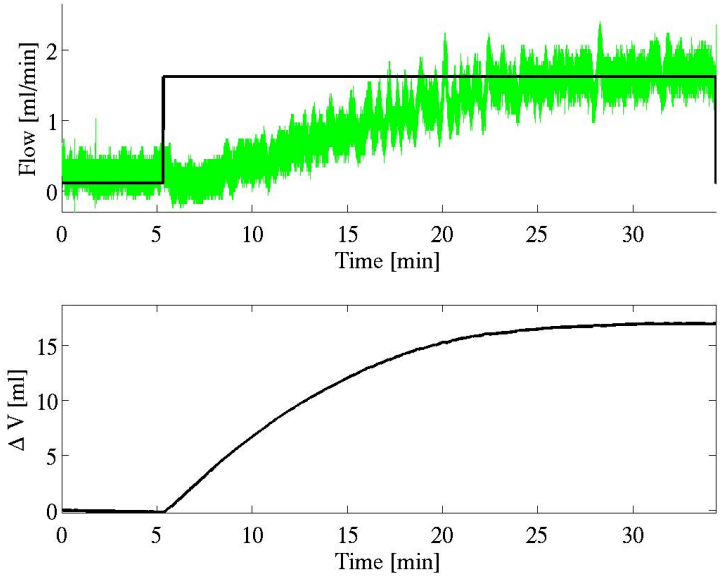

(b) Fluid Balance

Fig. 13: Plots for data set 02 version 1

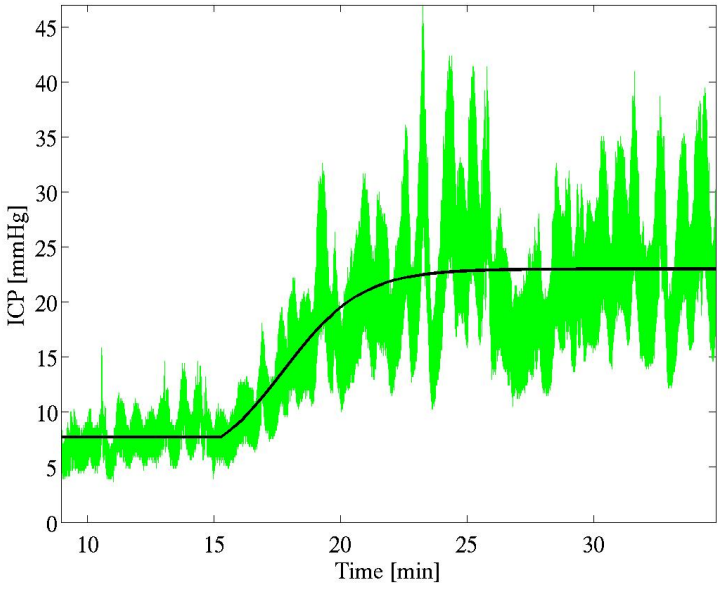

(a) Measured and fitted ICP

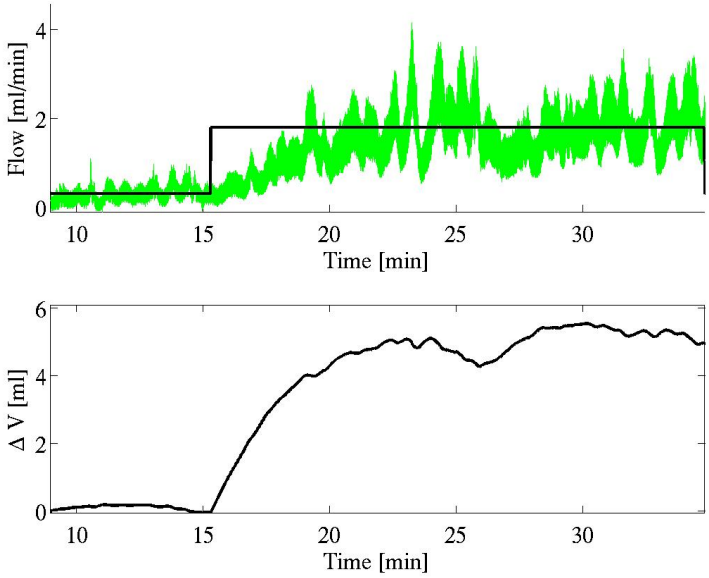

(b) Fluid Balance

Fig. 14: Plots for data set 03 version 1

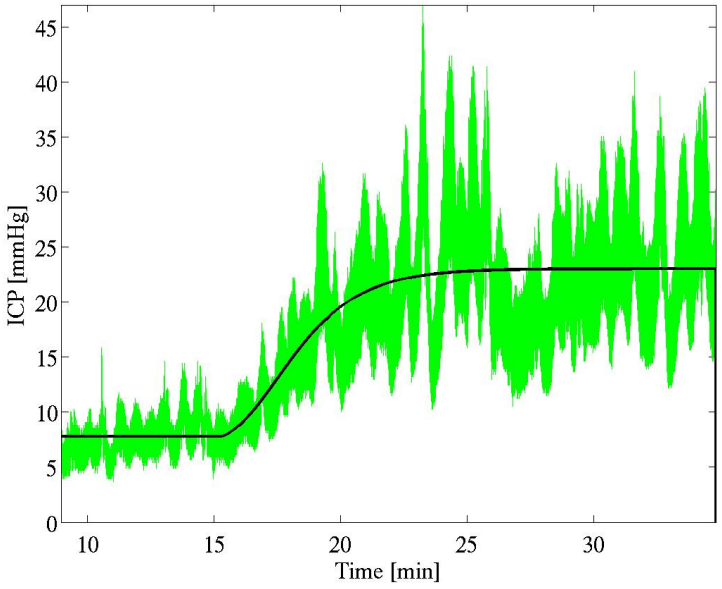

(a) Measured and fitted ICP

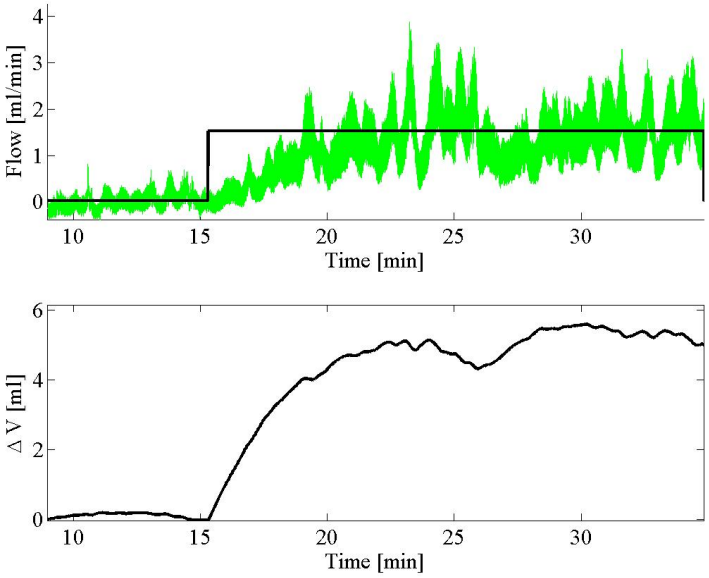

(b) Fluid Balance

Fig. 15: Plots for data set 03 version 2

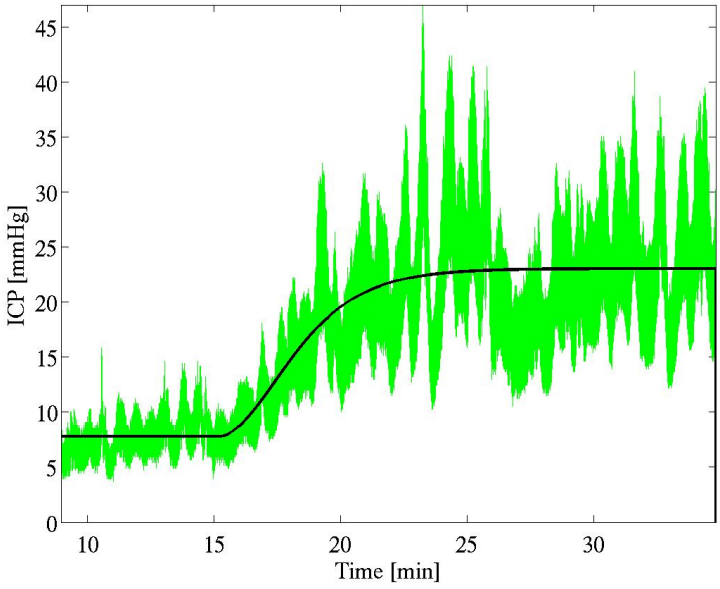

(a) Measured and fitted ICP

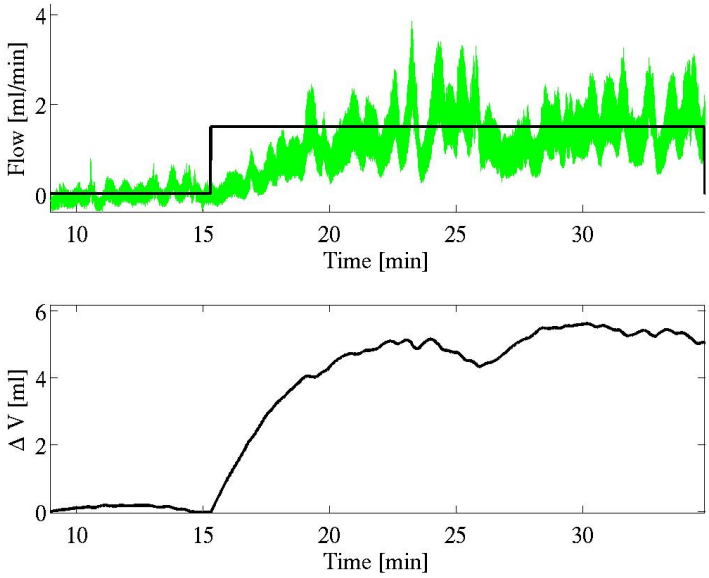

(b) Fluid Balance

Fig. 16: Plots for data set 03 version 3

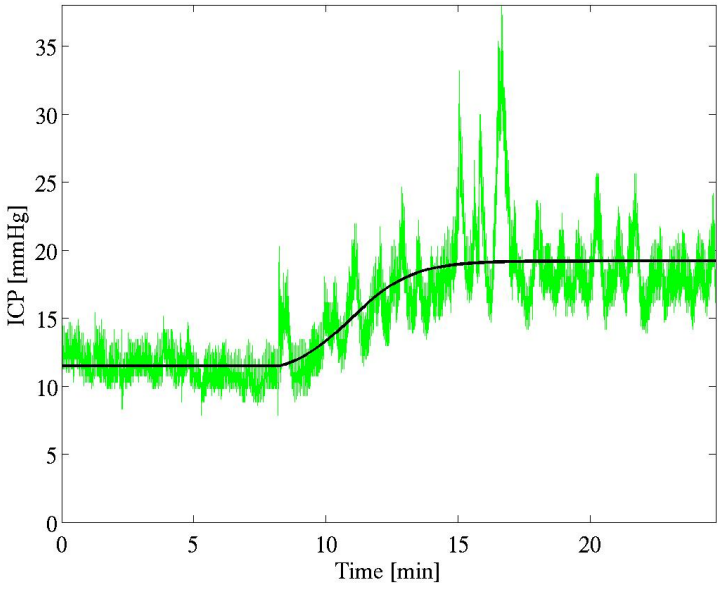

(a) Measured and fitted ICP

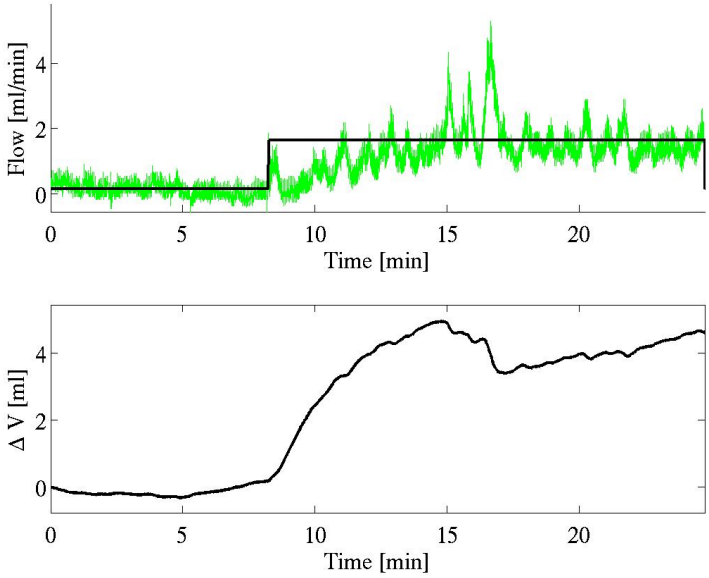

(b) Fluid Balance

Fig. 17: Plots for data set 04 version 1

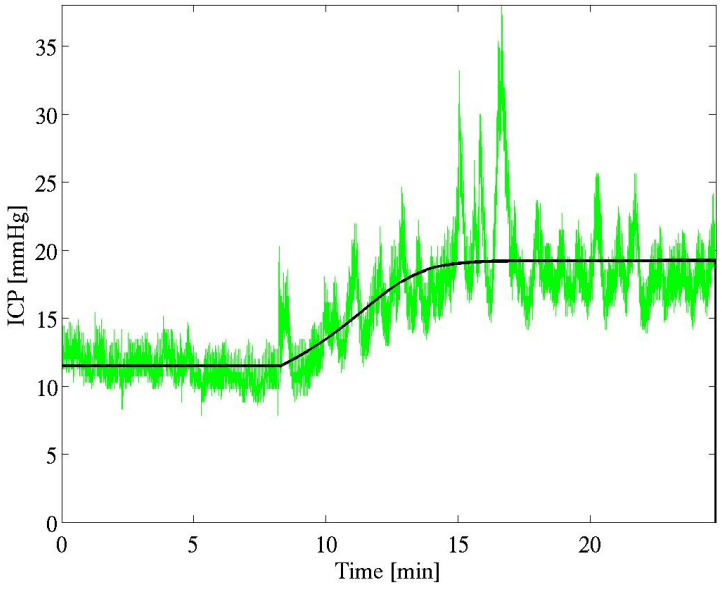

(a) Measured and fitted ICP

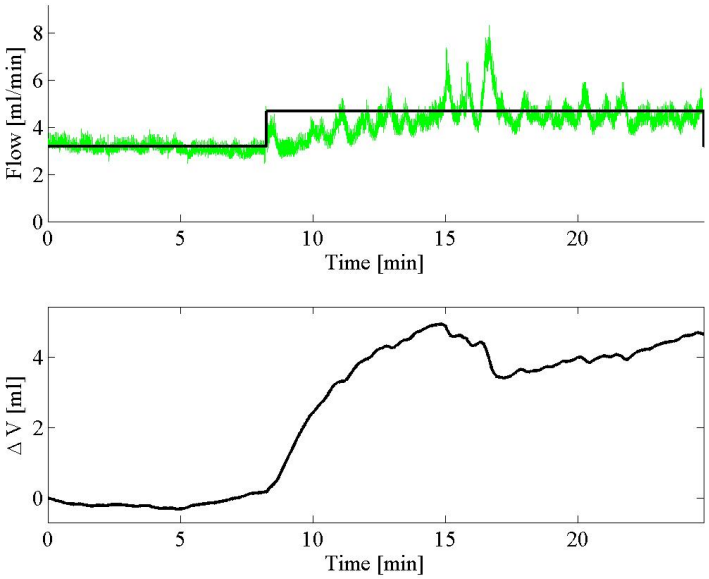

(b) Fluid Balance

Fig. 18: Plots for data set 04 version 2

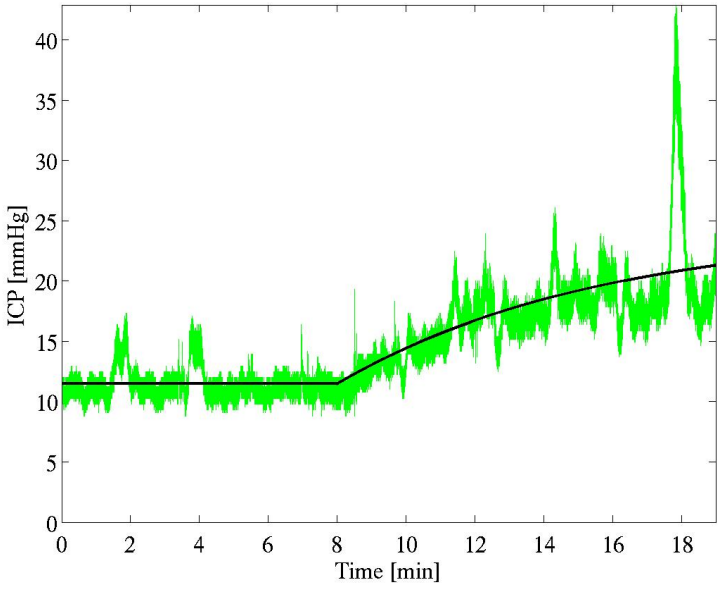

(a) Measured and fitted ICP

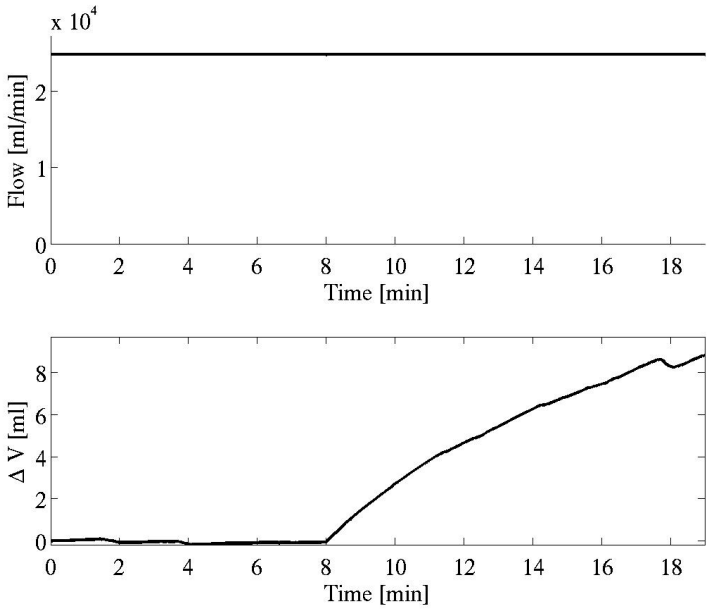

(b) Fluid Balance

Fig. 19: Plots for data set 05 version 1

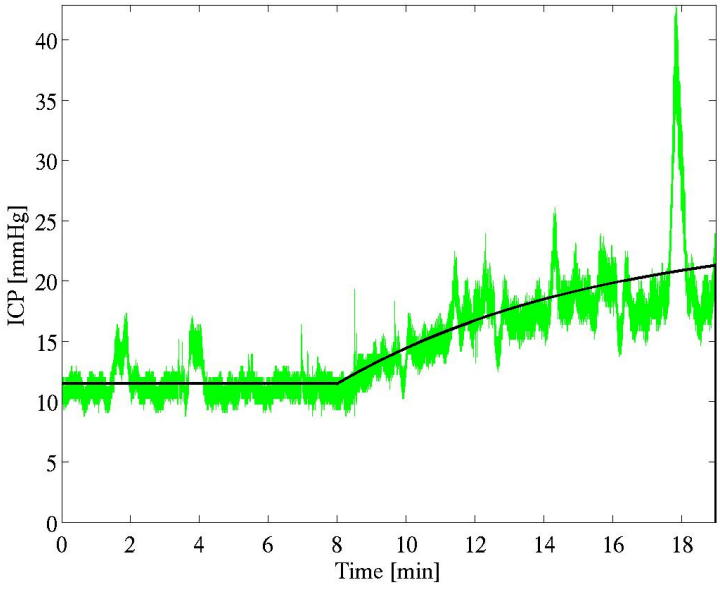

(a) Measured and fitted ICP

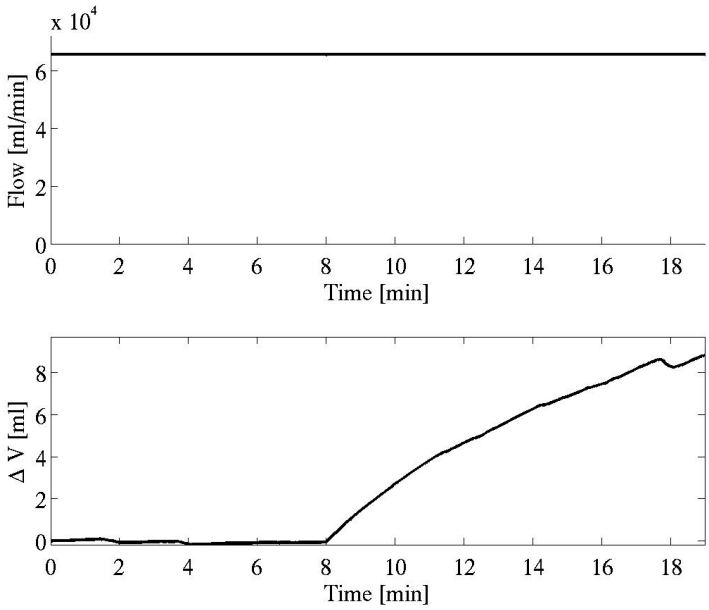

(b) Fluid Balance

Fig. 20: Plots for data set 05 version 3

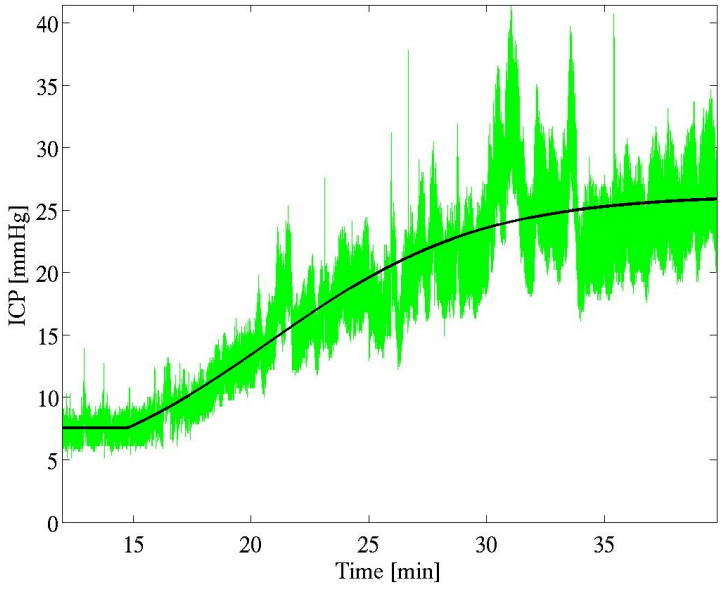

(a) Measured and fitted ICP

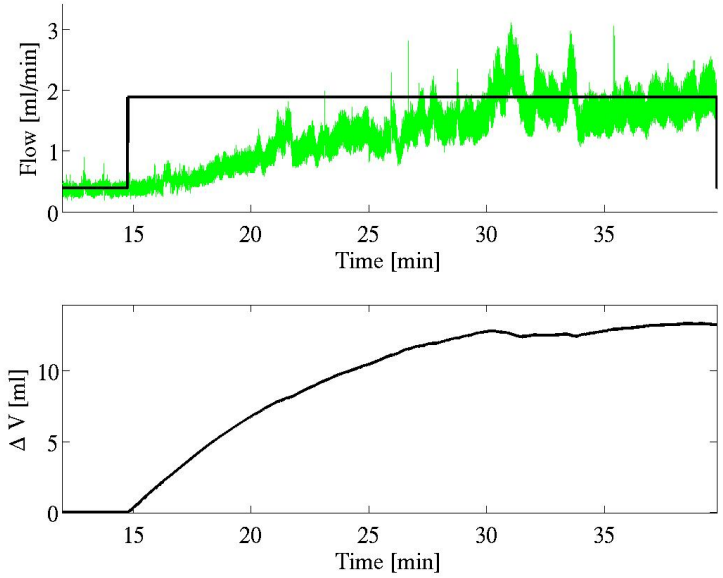

(b) Fluid Balance

Fig. 21: Plots for data set 06 version 1

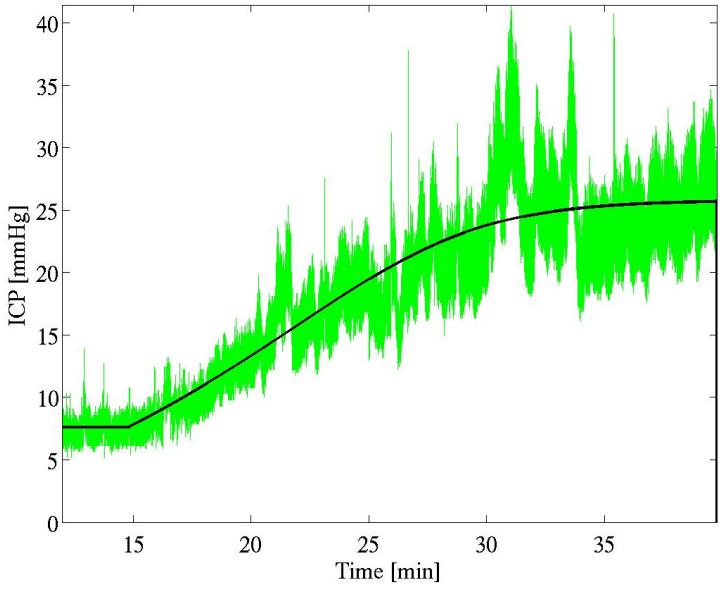

(a) Measured and fitted ICP

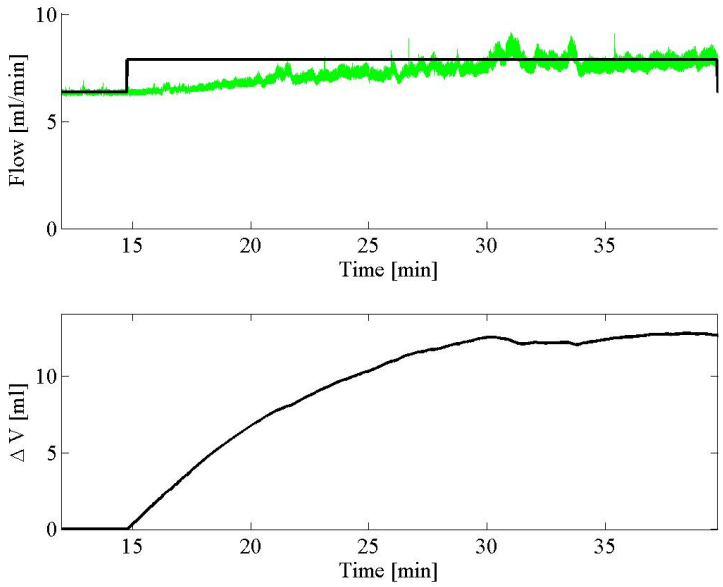

(b) Fluid Balance

Fig. 22: Plots for data set 06 version 2

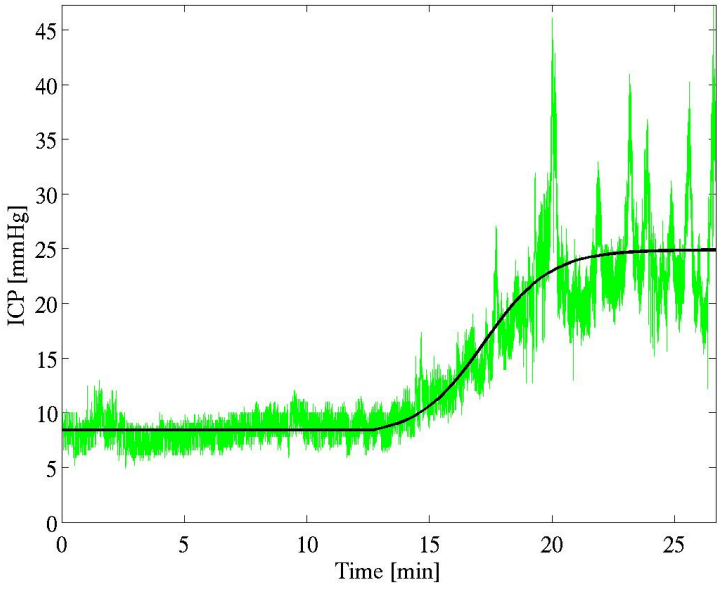

(a) Measured and fitted ICP

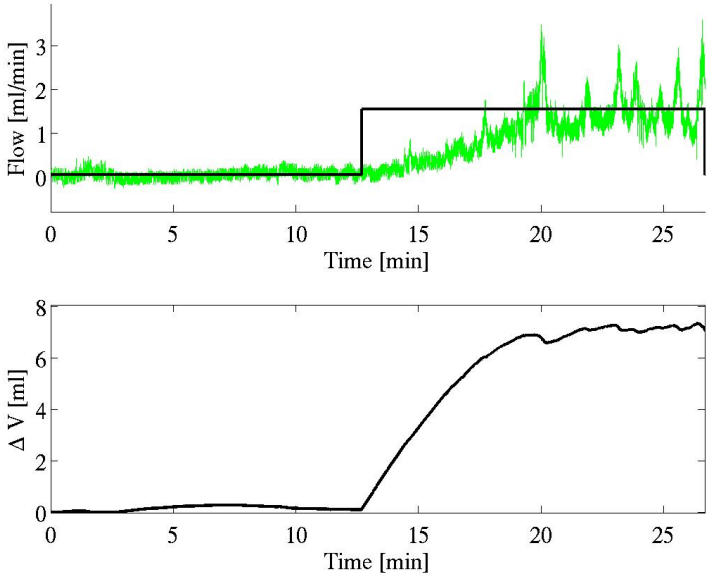

(b) Fluid Balance

Fig. 23: Plots for data set 07 version 1

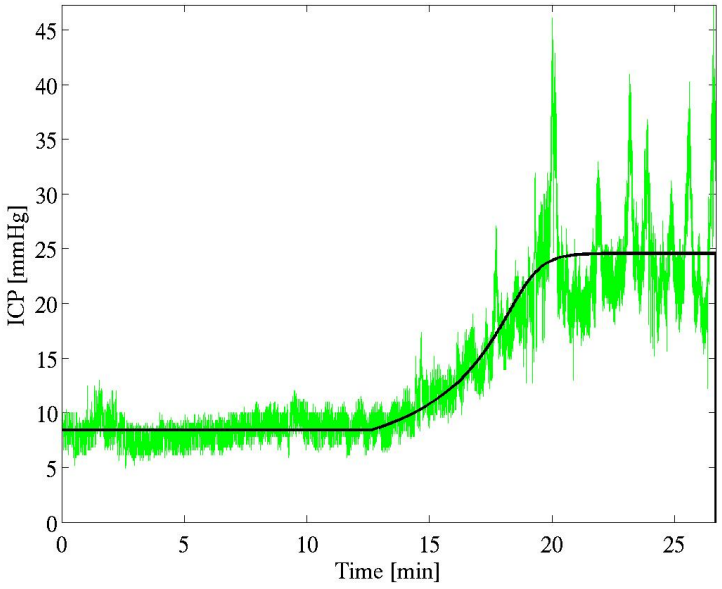

(a) Measured and fitted ICP

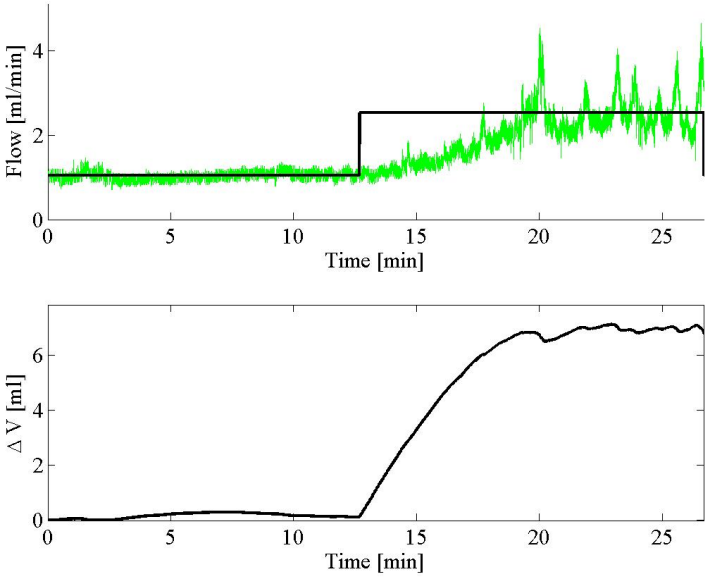

(b) Fluid Balance

Fig. 24: Plots for data set 07 version 2

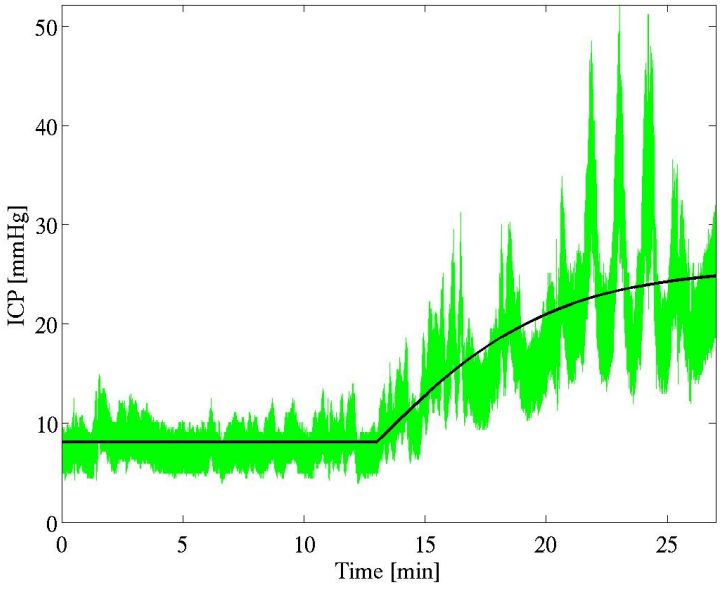

(a) Measured and fitted ICP

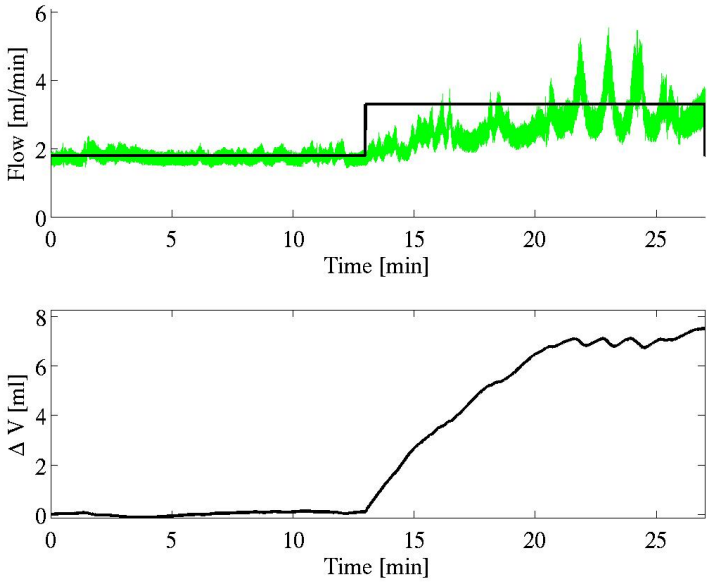

(b) Fluid Balance

Fig. 25: Plots for data set 08 version 1

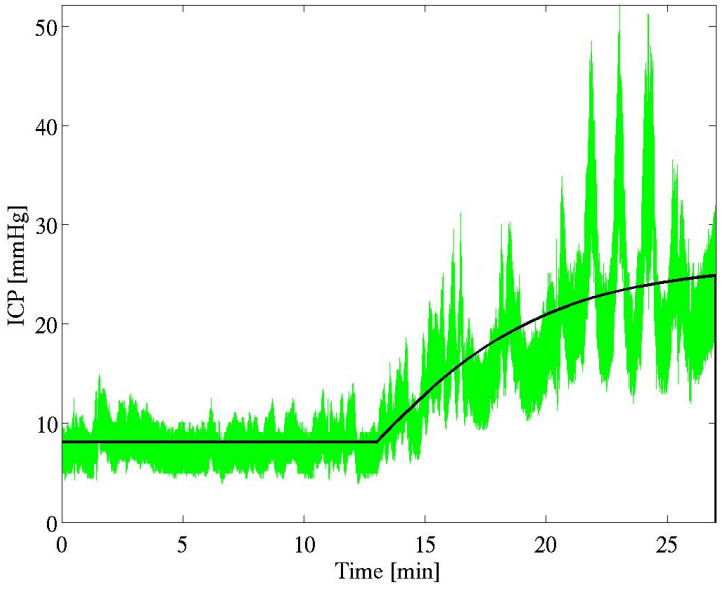

(a) Measured and fitted ICP

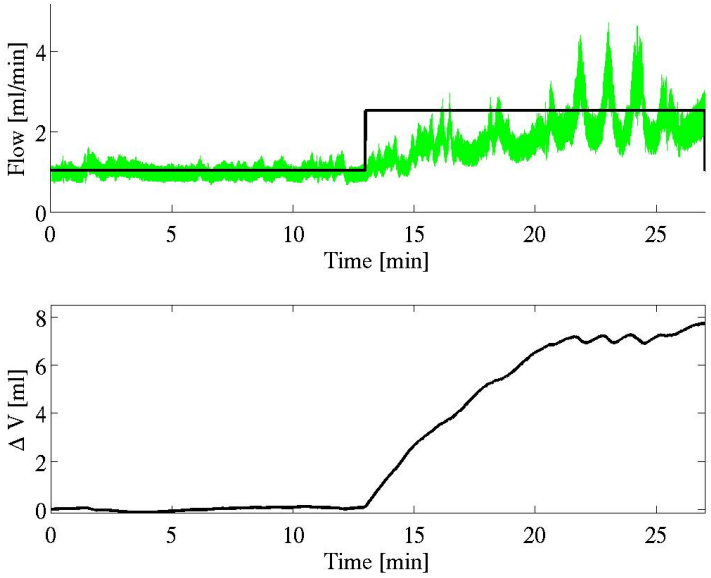

(b) Fluid Balance

Fig. 26: Plots for data set 08 version 3

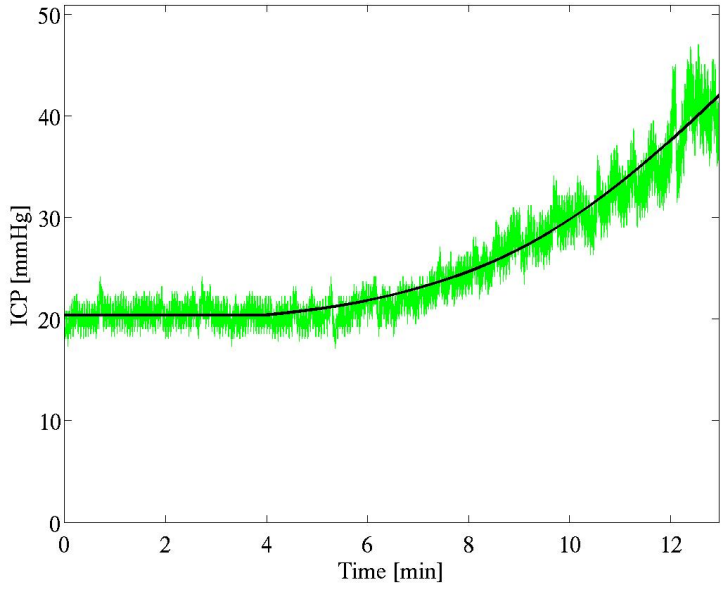

(a) Measured and fitted ICP

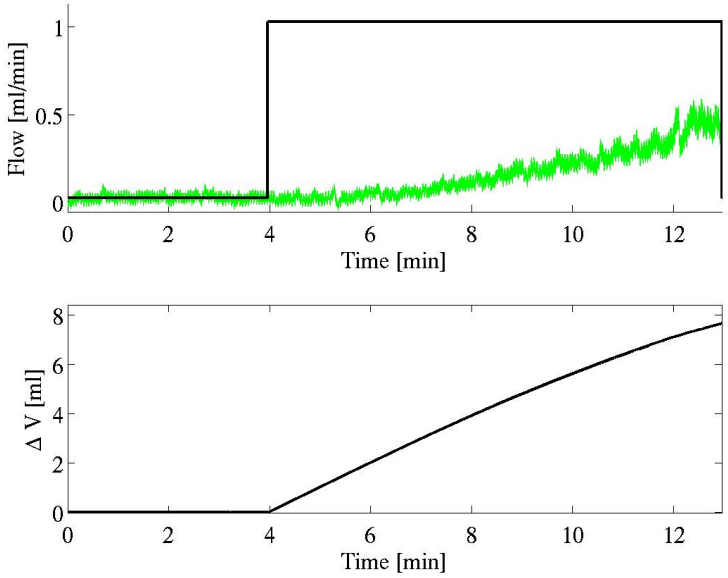

(b) Fluid Balance

Fig. 27: Plots for data set 09 version 1

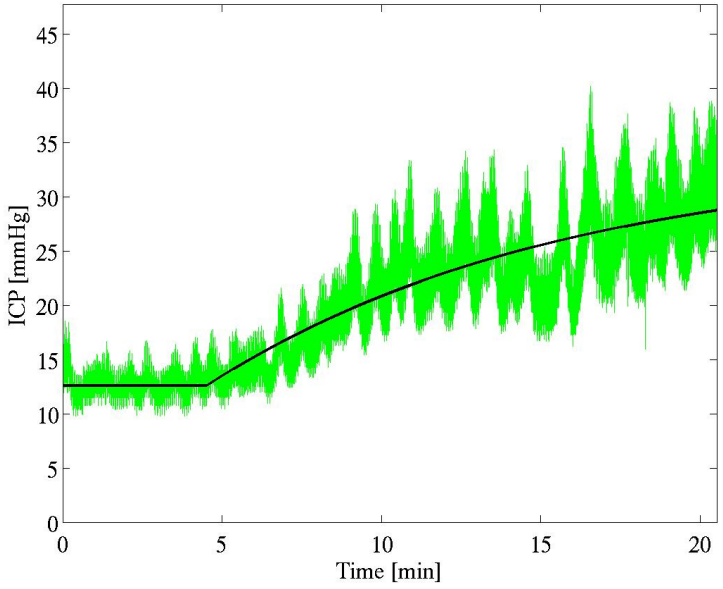

(a) Measured and fitted ICP

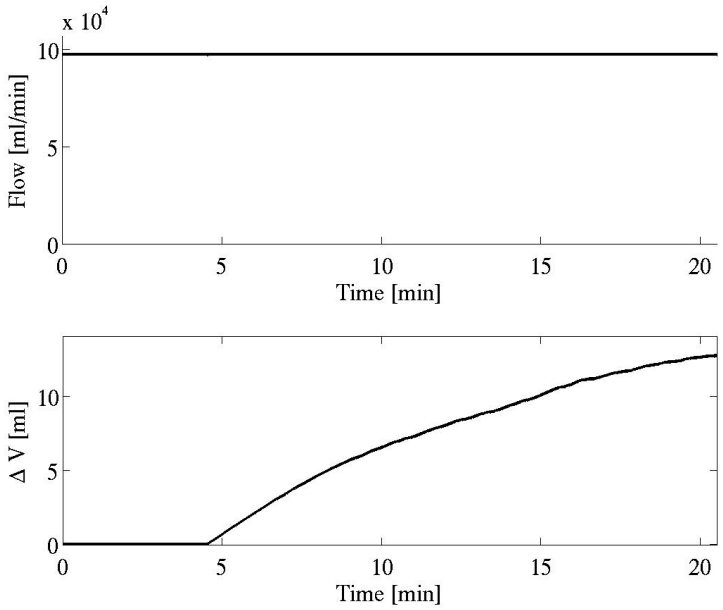

(b) Fluid Balance

Fig. 28: Plots for data set 10 version 1

A.2 Plots of Parameter Variations

This appendix contains the plots corresponding to §3.5 on page 13.

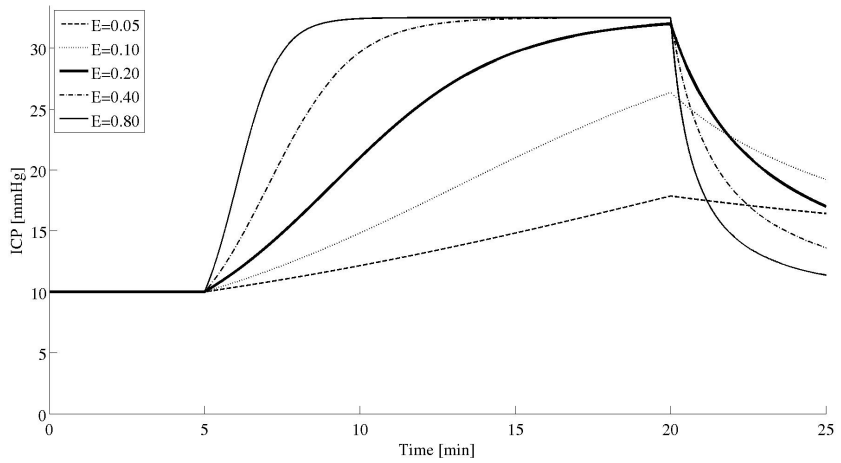

(a) Mean ICP

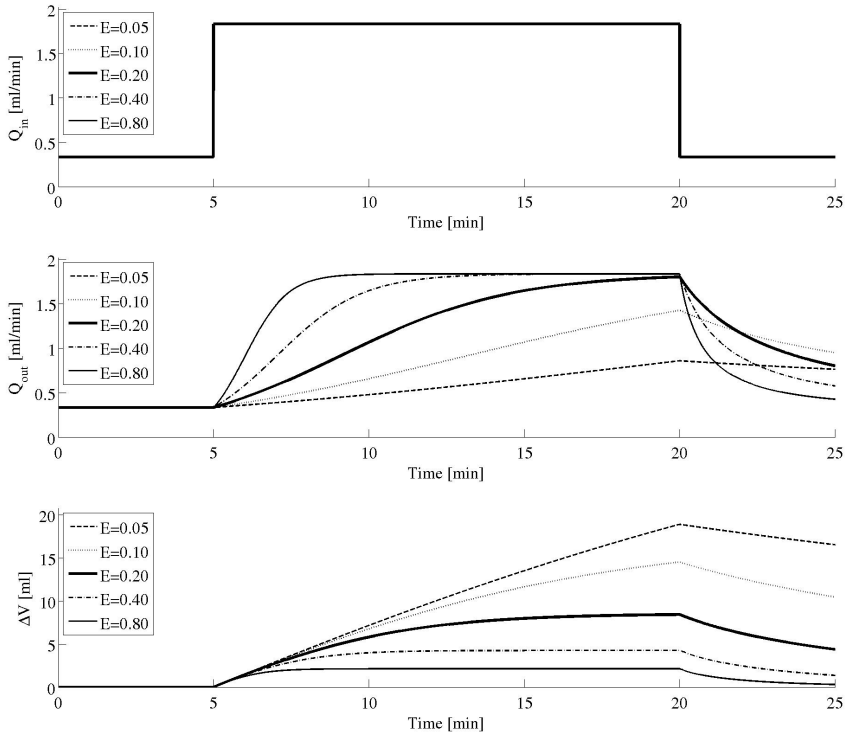

(b) Fluid flow and content

Fig. 29: Plots for variation of E in ml^{-1}

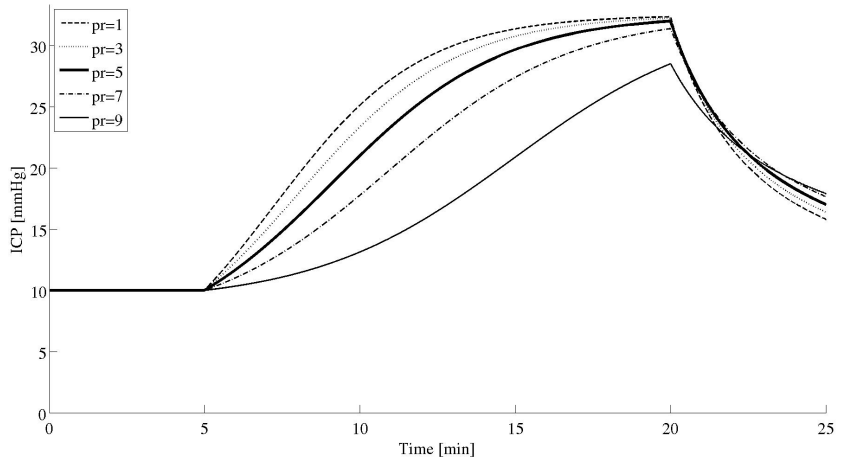

(a) Mean ICP

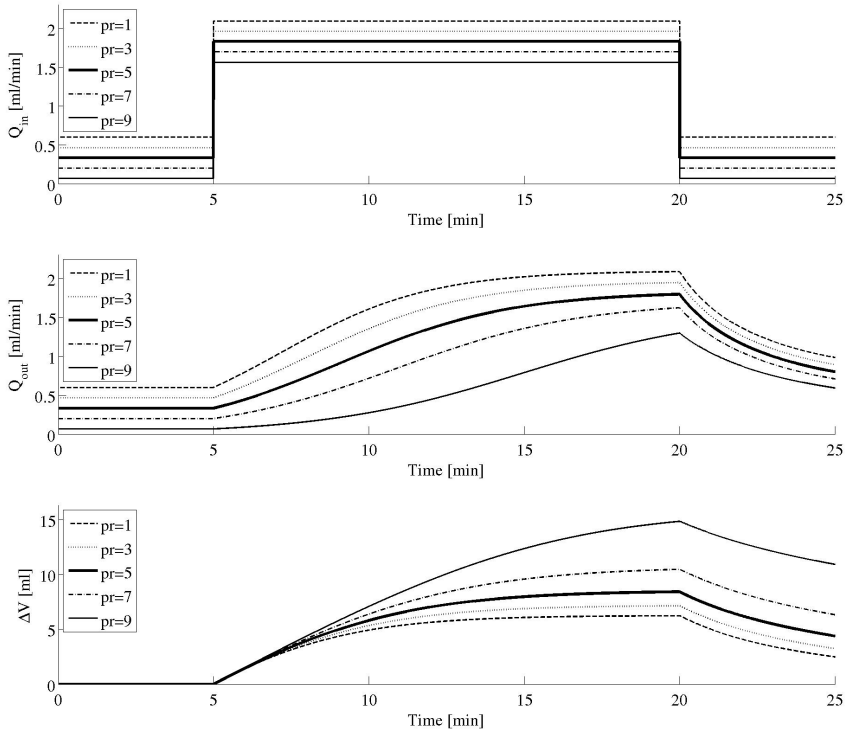

(b) Fluid flow and content

Fig. 30: Plots for variation of p_r in mmHg

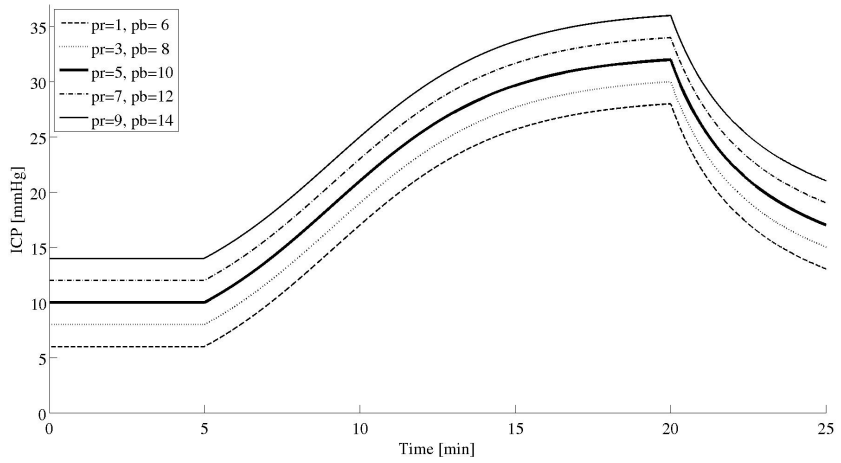

(a) Mean ICP

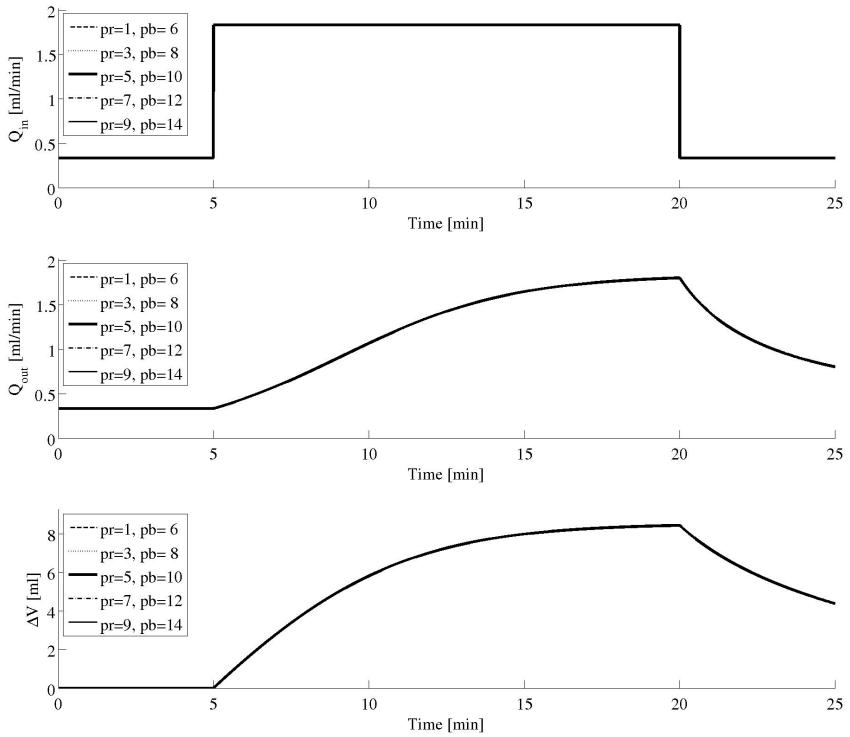

(b) Fluid flow and content

Fig. 31: Plots for variation of p_{b} and p_{r} in mmHg (with $p_{\mathrm{b}} - p_{\mathrm{r}}$ fixed)

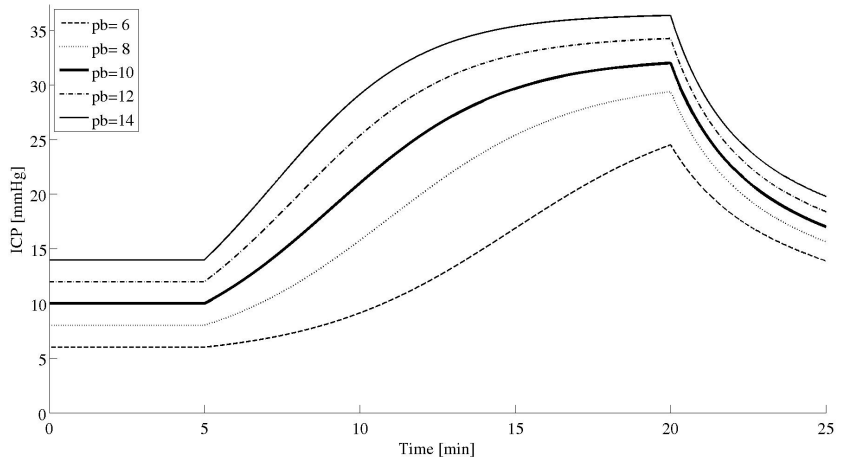

(a) Mean ICP

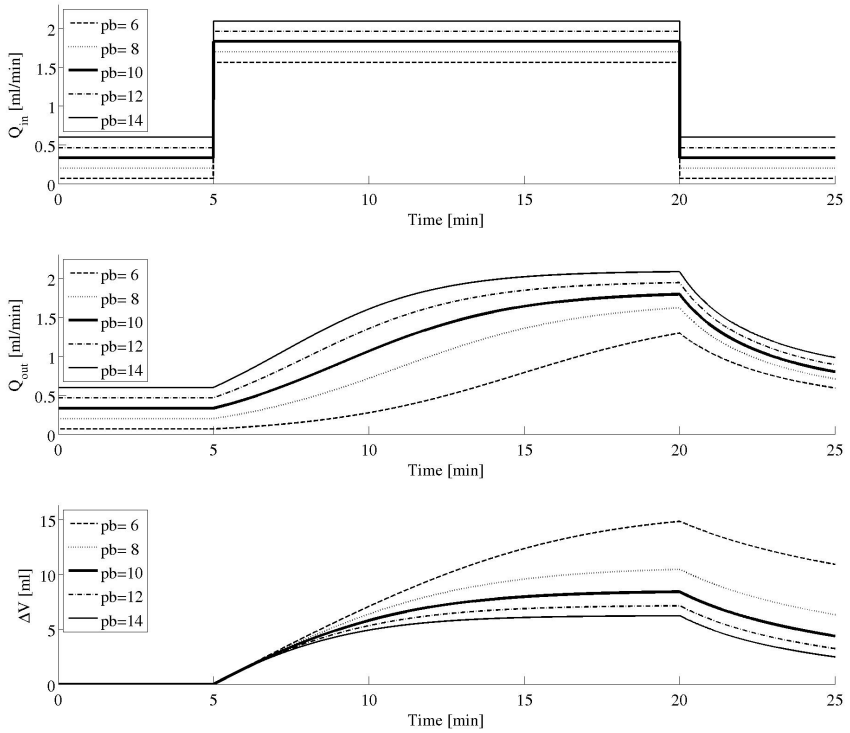

(b) Fluid flow and content

Fig. 32: Plots for variation of p_b in mmHg

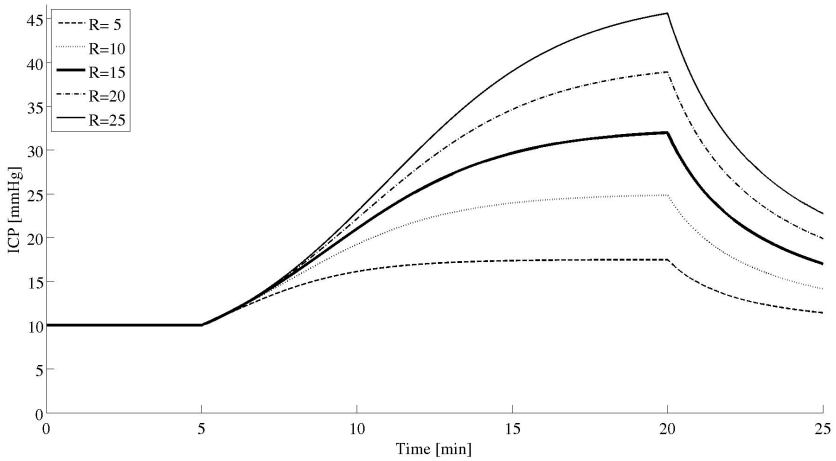

(a) Mean ICP

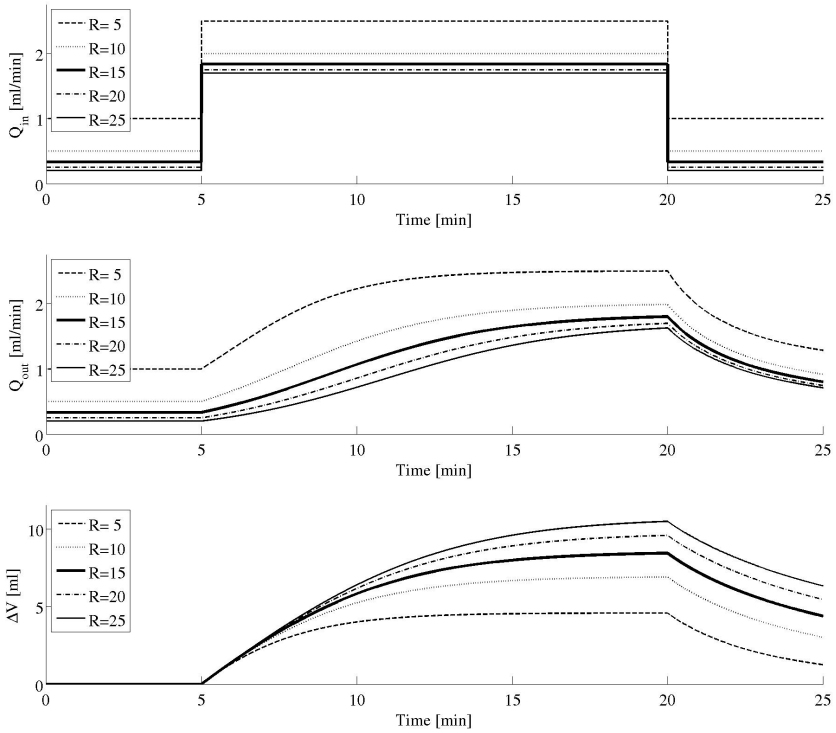

(b) Fluid flow and content

Fig. 33: Plots for variation of R in $\text{mmHg} \cdot \text{min} \cdot (\text{ml})^{-1}$

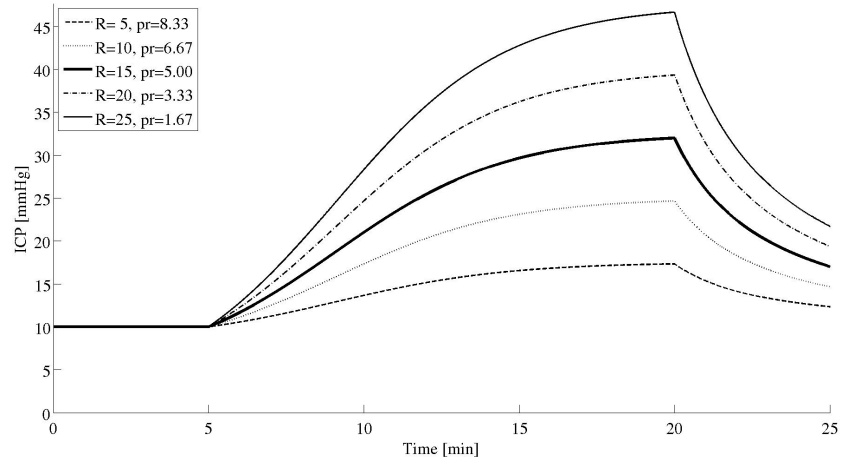

(a) Mean ICP

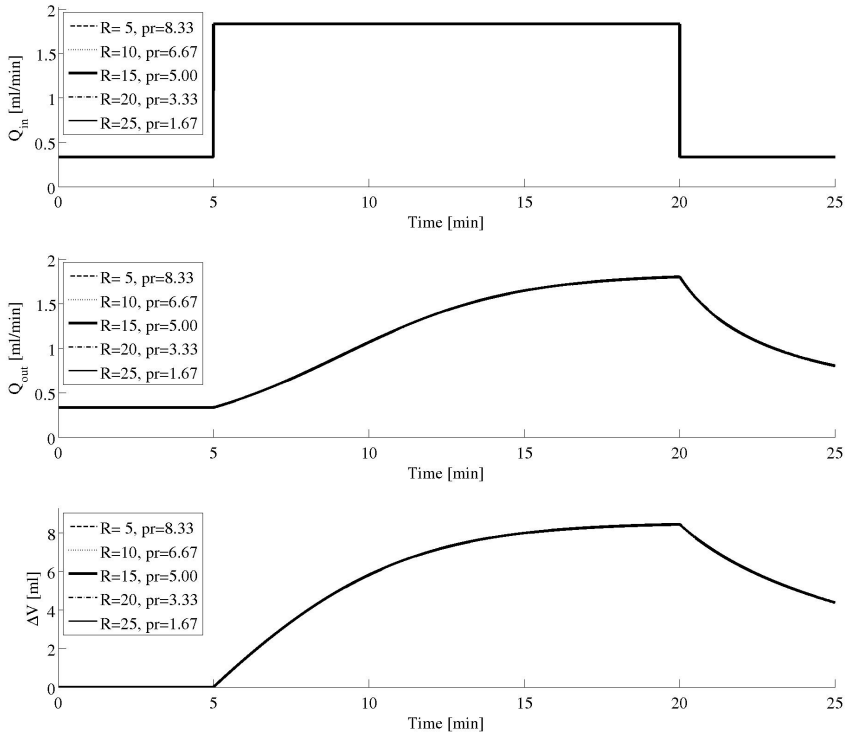

(b) Fluid flow and content

Fig. 34: Plots for variation of R and p_{r} (with $Q_{\mathrm{prod}} = \frac{p_{\mathrm{b}} - p_{\mathrm{r}}}{R}$ fixed)

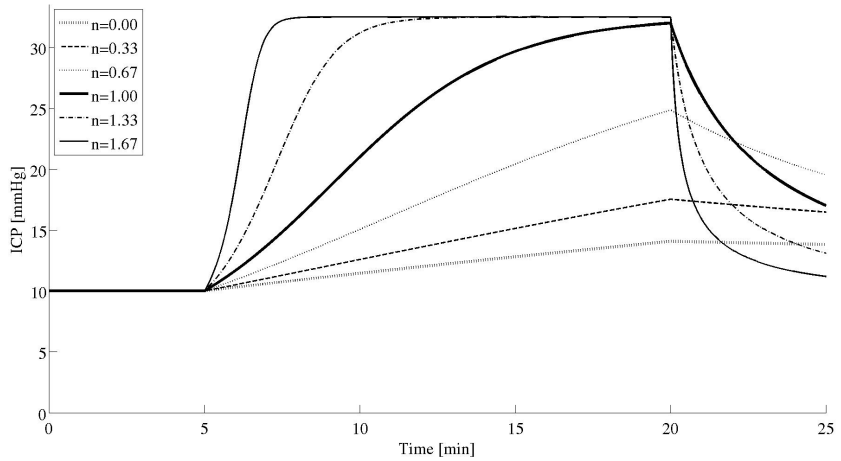

(a) Mean ICP

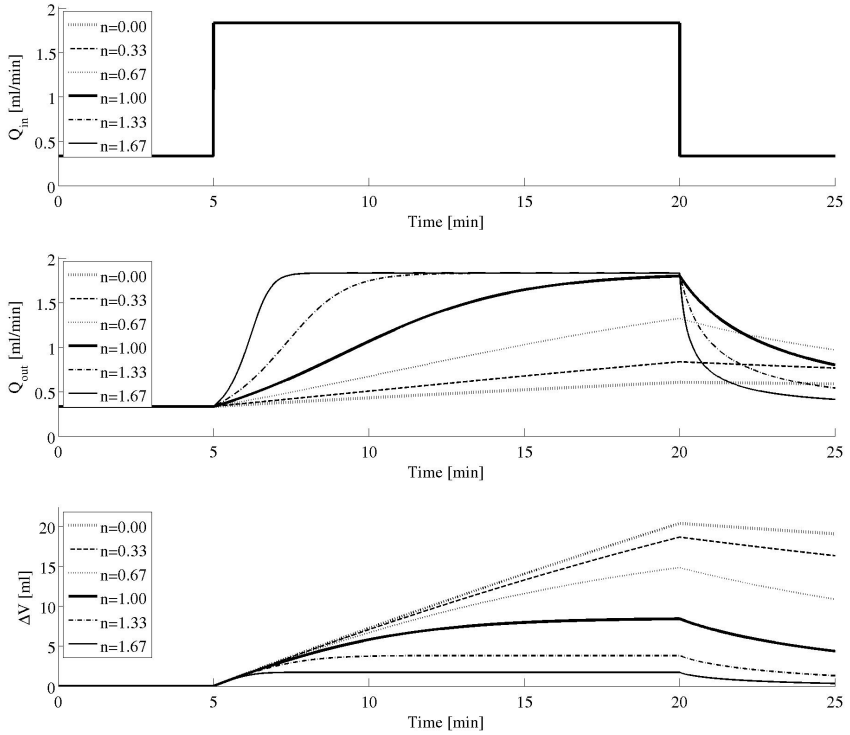

(b) Fluid flow and content

Fig. 35: Plots for variation of n

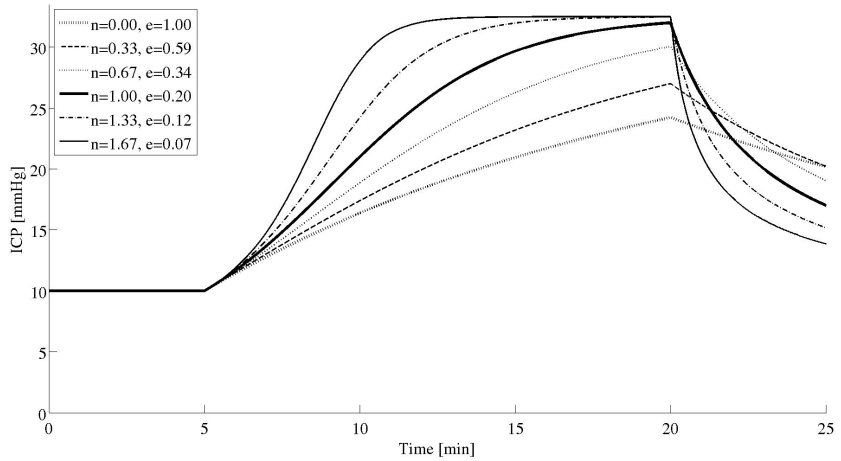

(a) Mean ICP

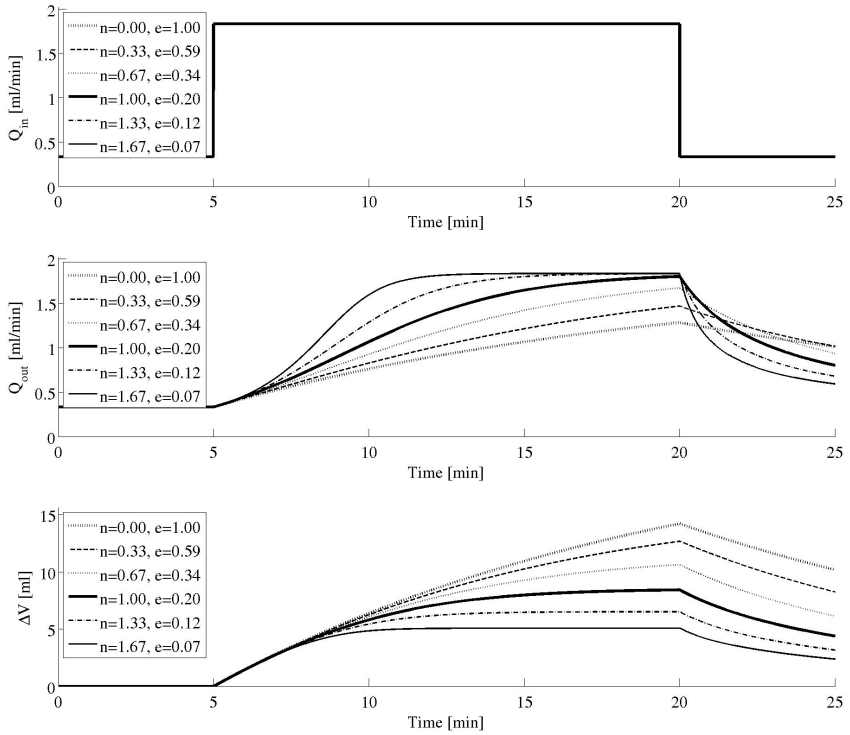

(b) Fluid flow and content

Fig. 36: Plots for variation of n and $\tilde{e}$, (with $E(p_{\mathrm{b}}) = \tilde{e}\,(p_{\mathrm{b}} - p_{\mathrm{r}})^{n-1}$ fixed)

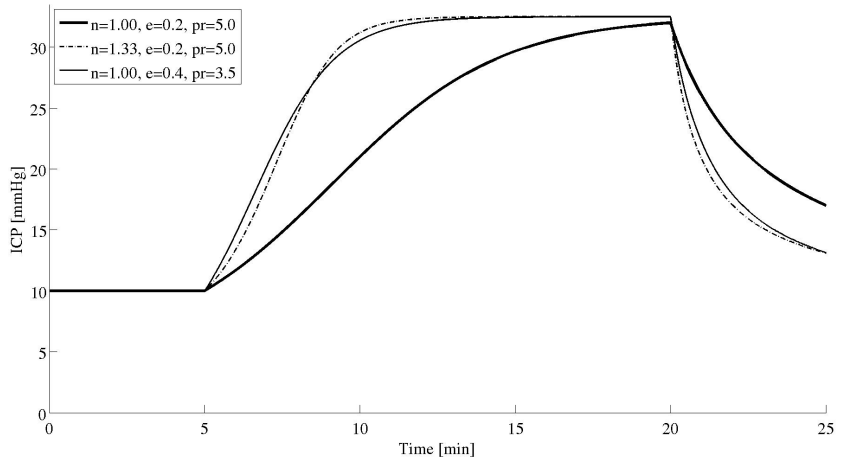

(a) Mean ICP

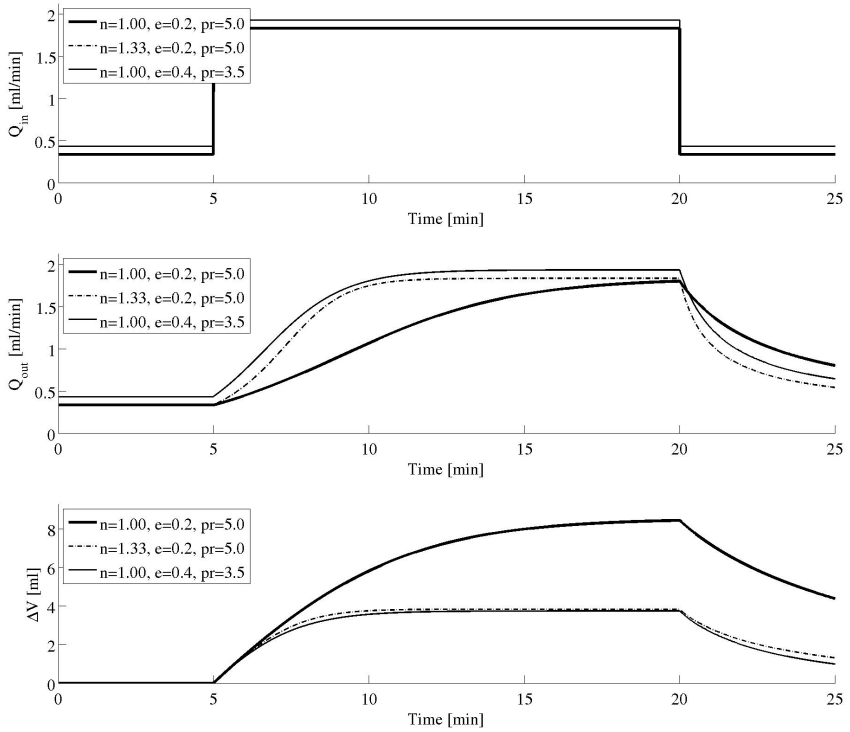

(b) Fluid flow and content

Fig. 37: Plots for variation of n, $\tilde{e}$ and pr

A.3 Details of Finite Element Simulation

Here, we give details of the finite element implementation for (20) in §4.4. The whole system of equations was solved using Matlab's backslash operator.

For $j = 1, \ldots, N-1$, φ vanishes at the boundary, hence

$$\begin{aligned}
A\left(\begin{pmatrix}\hat{\varepsilon}\\ \hat{p}\end{pmatrix}, \varphi_j\right) &= \int_0^1 (\hat{\varepsilon} - a_1\hat{p})\,\varphi_j' \mathrm{d}\xi \\
&= \int_{\xi_{j-1}}^{\xi_j} (\hat{\varepsilon} - a_1\hat{p})\,\varphi_j' \mathrm{d}\xi + \int_{\xi_j}^{\xi_{j+1}} (\hat{\varepsilon} - a_1\hat{p})\,\varphi_j' \mathrm{d}\xi \\
&= \frac{1}{h_j}\int_{\xi_{j-1}}^{\xi_j} (\hat{\varepsilon} - a_1\hat{p})\,\mathrm{d}\xi - \frac{1}{h_{j+1}}\int_{\xi_j}^{\xi_{j+1}} (\hat{\varepsilon} - a_1\hat{p})\,\mathrm{d}\xi \\
&= \frac{h_j}{2h_j}\left(\varepsilon_{j-1} - a_1 p_{j-1} + \varepsilon_j - a_1 p_j\right) - \frac{h_{j+1}}{2h_{j+1}}\left(\varepsilon_j - a_1 p_j + \varepsilon_{j+1} - a_1 p_{j+1}\right) \\
&= \frac{1}{2}\left(\varepsilon_{j-1} - a_1 p_{j-1}\right) - \frac{1}{2}\left(\varepsilon_{j+1} - a_1 p_{j+1}\right)
\end{aligned}$$

Now consider $j = N$

$$\begin{aligned}
A\left(\begin{pmatrix}\hat{\varepsilon}\\ \hat{p}\end{pmatrix}, \varphi_N\right) &= \int_0^1 (\hat{\varepsilon} - a_1\hat{p})\,\varphi_N' \mathrm{d}\xi - \left[(\hat{\varepsilon} - a_1\hat{p})\,\varphi_N\right]_0^1 \\
&= \int_{\xi_{N-1}}^{\xi_N} (\hat{\varepsilon} - a_1\hat{p})\,\varphi_N' \mathrm{d}\xi - \left[(\hat{\varepsilon} - a_1\hat{p})\,\varphi_N\right]_{\xi_0}^{\xi_N} \\
&= \frac{1}{h_N}\frac{h_N}{2}\left(\epsilon_{N-1} - a_1 p_{N-1} + \epsilon_N - a_1 p_N\right) - \left(\epsilon_N - a_1 p_N\right) \\
&= \frac{1}{2}\left(\varepsilon_{N-1} - a_1 p_{N-1}\right) - \frac{1}{2}\left(\varepsilon_N - a_1 p_N\right).
\end{aligned}$$

So, now consider for $j = 1, \ldots, N-1$

$$\begin{aligned}
B\left(\begin{pmatrix}\hat{\varepsilon}\\ \hat{p}\end{pmatrix}, \varphi_j\right) &= \int_0^1 e^{M\hat{\varepsilon}}\hat{p}'\varphi_j' \mathrm{d}\xi = \int_0^1 e^{M\hat{\varepsilon}}\left(\sum_{k=0}^{N} \mathrm{p}_k \varphi_k'\right)\varphi_j' \mathrm{d}\xi \\
&= \int_{\xi_{j-1}}^{\xi_j} e^{M\hat{\varepsilon}}\left(\mathrm{p}_{j-1}\varphi_{j-1}' + \mathrm{p}_j\varphi_j'\right)\varphi_j' \mathrm{d}\xi \\
&\quad + \int_{\xi_j}^{\xi_{j+1}} e^{M\hat{\varepsilon}}\left(\mathrm{p}_j\varphi_j' + \mathrm{p}_{j+1}\varphi_{j+1}'\right)\varphi_j' \mathrm{d}\xi \\
&= \frac{\mathrm{p}_j - \mathrm{p}_{j-1}}{h_j^2}\underbrace{\int_{\xi_{j-1}}^{\xi_j} e^{M\hat{\varepsilon}}\mathrm{d}\xi}_{=I_j^B} - \frac{\mathrm{p}_{j+1} - \mathrm{p}_j}{h_{j+1}^2}\underbrace{\int_{\xi_j}^{\xi_{j+1}} e^{M\hat{\varepsilon}}\mathrm{d}\xi}_{=I_{j+1}^B}
\end{aligned}$$

with

$$I_j^B := \int_{\xi_{j-1}}^{\xi_j} e^{M\hat{\varepsilon}} \mathrm{d}\xi \qquad = \int_0^{h_j} e^{M\left(\epsilon_{j-1}+\xi\frac{\epsilon_j-\epsilon_{j-1}}{h_j}\right)} \mathrm{d}\xi = \frac{h_j}{M(\epsilon_j-\epsilon_{j-1})}\left(e^{M\epsilon_j}-e^{M\epsilon_{j-1}}\right).$$

This is numerically unstable when $(\epsilon_j - \epsilon_{j-1})$ approaches zero. Instead we will compute the integral numerically using Gauss quadrature,

$$I_j^B = \frac{h_j}{2}\int_{-1}^{1} e^{\frac{M}{2}\left(\epsilon_{j-1}(1-s)+\epsilon_j(1+s)\right)}\mathrm{d}s \approx \frac{h_j}{2}\sum_{g\in G} w_g e^{\frac{M}{2}\left(\epsilon_{j-1}(1-s_g)+\epsilon_j(1+s_g)\right)}$$

with, e. g., $G = \{1,\dots,5\}$,

$$\left(s_g\right)_g = \begin{pmatrix} -\frac{1}{3}\sqrt{5+2\sqrt{\frac{10}{7}}} \\ -\frac{1}{3}\sqrt{5-2\sqrt{\frac{10}{7}}} \\ 0 \\ \frac{1}{3}\sqrt{5-2\sqrt{\frac{10}{7}}} \\ \frac{1}{3}\sqrt{5+2\sqrt{\frac{10}{7}}} \end{pmatrix}, \qquad \left(w_g\right)_g = \begin{pmatrix} \frac{322-13\sqrt{70}}{900} \\ \frac{322+13\sqrt{70}}{900} \\ \frac{128}{225} \\ \frac{322+13\sqrt{70}}{900} \\ \frac{322-13\sqrt{70}}{900} \end{pmatrix}.$$

Hence, we receive

$$\begin{aligned} B\left(\begin{pmatrix}\hat{\varepsilon}\\ \hat{p}\end{pmatrix}, \varphi_j\right) \approx{}& \frac{\mathrm{p}_j - \mathrm{p}_{j-1}}{2h_j}\sum_{g\in G} w_g e^{\frac{M}{2}\left(\epsilon_{j-1}(1-s_g)+\epsilon_j(1+s_g)\right)} \\ &- \frac{\mathrm{p}_{j+1} - \mathrm{p}_j}{2h_{j+1}}\sum_{g\in G} w_g e^{\frac{M}{2}\left(\epsilon_j(1-s_g)+\epsilon_{j+1}(1+s_g)\right)}. \end{aligned}$$

The linearisation of B is given by

$$\mathcal{D}B\left(\begin{pmatrix}\hat{\varepsilon}\\ \hat{p}\end{pmatrix}; \begin{pmatrix}\Delta\hat{\varepsilon}\\ \Delta\hat{p}\end{pmatrix}, \varphi_j\right) = B\left(\begin{pmatrix}\hat{\varepsilon}\\ \Delta\hat{p}\end{pmatrix}, \varphi_j\right) + M\int_0^1 e^{M\hat{\varepsilon}}\Delta\hat{\varepsilon}\hat{p}'\varphi_j' \mathrm{d}\xi,$$

where

$$\begin{aligned} M\int_0^1 e^{M\hat{\varepsilon}}\Delta\hat{\varepsilon}\hat{p}'\varphi_j'\mathrm{d}\xi &= M\int_{\xi_{j-1}}^{\xi_j} e^{M\hat{\varepsilon}}\Delta\hat{\varepsilon}\hat{p}'\varphi_j'\mathrm{d}\xi + M\int_{\xi_j}^{\xi_{j+1}} e^{M\hat{\varepsilon}}\Delta\hat{\varepsilon}\hat{p}'\varphi_j'\mathrm{d}\xi \\ &= \frac{\mathrm{p}_j - \mathrm{p}_{j-1}}{h_j^2}\underbrace{M\int_{\xi_{j-1}}^{\xi_j} e^{M\hat{\varepsilon}}\Delta\hat{\varepsilon}\mathrm{d}\xi}_{=h_j I_j^{\mathcal{D}B}} - \frac{\mathrm{p}_{j+1} - \mathrm{p}_j}{h_{j+1}^2}\underbrace{M\int_{\xi_j}^{\xi_{j+1}} e^{M\hat{\varepsilon}}\Delta\hat{\varepsilon}\mathrm{d}\xi}_{=h_{j+1} I_{j+1}^{\mathcal{D}B}} \end{aligned}$$

with

$$\begin{aligned}
I_j^{\mathcal{D}B} &:= \frac{M}{h_j}\int_{\xi_{j-1}}^{\xi_j} e^{M\hat{\varepsilon}}\Delta\hat{\varepsilon}\mathrm{d}\xi \\
&= \frac{M}{h_j}\int_0^{h_j} e^{M\epsilon_{j-1}+\frac{M}{h_j}(\epsilon_j-\epsilon_{j-1})\xi}\left(M\Delta\epsilon_{j-1}+\frac{M}{h_j}(\Delta\epsilon_j-\Delta\epsilon_{j-1})\xi\right)\mathrm{d}\xi \\
&= -\frac{1}{\epsilon_j-\epsilon_{j-1}}\int_0^{h_j} e^{M\epsilon_{j-1}+\frac{M}{h_j}(\epsilon_j-\epsilon_{j-1})\xi}\left(\frac{M}{h_j}(\Delta\epsilon_j-\Delta\epsilon_{j-1})\right)\mathrm{d}\xi \\
&\quad + \left[\frac{1}{\epsilon_j-\epsilon_{j-1}}e^{M\epsilon_{j-1}+\frac{M}{h_j}(\epsilon_j-\epsilon_{j-1})\xi}\left(M\Delta\epsilon_{j-1}+\frac{M}{h_j}(\Delta\epsilon_j-\Delta\epsilon_{j-1})\xi\right)\right]_0^{h_j} \\
&= -\frac{\left(e^{M\epsilon_j}-e^{M\epsilon_{j-1}}\right)}{(\epsilon_j-\epsilon_{j-1})^2}(\Delta\epsilon_j-\Delta\epsilon_{j-1})+\frac{M}{(\epsilon_j-\epsilon_{j-1})}\left(e^{M\epsilon_j}\Delta\epsilon_j-e^{M\epsilon_{j-1}}\Delta\epsilon_{j-1}\right).
\end{aligned}$$

Again we encounter numerical instabilities, thus integrate using Gauss quadrature and obtain

$$I_j^{\mathcal{D}B} \approx \frac{M}{4}\sum_{g\in G} w_g e^{\frac{M}{2}\left(\epsilon_{j-1}(1-s_g)+\epsilon_j(1+s_g)\right)}\left(\Delta\epsilon_{j-1}(1-s_g)+\Delta\epsilon_j(1+s_g)\right).$$

Then

$$\mathcal{D}B\left(\begin{pmatrix}\hat{\varepsilon}\\ \hat{p}\end{pmatrix};\begin{pmatrix}\Delta\hat{\varepsilon}\\ \Delta\hat{p}\end{pmatrix},\varphi_j\right) = B\left(\begin{pmatrix}\hat{\varepsilon}\\ \Delta\hat{p}\end{pmatrix},\varphi_j\right)+\frac{\left(\mathrm{p}_j-\mathrm{p}_{j-1}\right)}{h_j}I_j^{\mathcal{D}B}-\frac{\left(\mathrm{p}_{j+1}-\mathrm{p}_j\right)}{h_{j+1}}I_{j+1}^{\mathcal{D}B}.$$

Finally, consider the boundary conditions

$$C\left(\begin{pmatrix}\hat{\varepsilon}\\ \hat{p}\end{pmatrix}\right) := \begin{pmatrix}a_5\hat{p}'(0)e^{M\hat{\varepsilon}(0)}+Q\\ \hat{\varepsilon}(0)+a_6\hat{p}(0)\\ \hat{p}(1)-p_s\end{pmatrix} = \begin{pmatrix}a_5\frac{\mathrm{p}_1-\mathrm{p}_0}{h_1}e^{M\epsilon_0}+Q\\ \epsilon_0+a_6\mathrm{p}_0\\ \mathrm{p}_N-p_s\end{pmatrix}$$

and their linearisations

$$\begin{aligned}
\mathcal{D}C\left(\begin{pmatrix}\varepsilon\\ p\end{pmatrix};\begin{pmatrix}\Delta\varepsilon\\ \Delta p\end{pmatrix}\right) &= \begin{pmatrix}a_5e^{M\varepsilon(0)}\left[\Delta p'(0)+Mp'(0)\Delta\varepsilon(0)\right]\\ \Delta\varepsilon(0)+a_6\Delta p(0)\\ \Delta p(1)\end{pmatrix} \\
&= \begin{pmatrix}\frac{a_5}{h_1}e^{M\epsilon_0}\left[(\Delta\mathrm{p}_1-\Delta\mathrm{p}_0)+M(\mathrm{p}_1-\mathrm{p}_0)\Delta\epsilon_0\right]\\ \Delta\epsilon_0+a_6\Delta\mathrm{p}_0\\ \Delta\mathrm{p}_N\end{pmatrix}.
\end{aligned}$$